# Condensation of the *Drosophila* Nerve Cord is Oscillatory and depends on Coordinated Mechanical Interactions

Katerina Karkali[1], Prabhat Tiwari[2], Anand Singh[2#], Sham Tlili[2#], Ignasi Jorba[3,4,5], Daniel Navajas[3,4,5], José J. Muñoz[6,7,8*], Timothy E. Saunders[2,9,10*] and Enrique Martin-Blanco[1,*§]

[1] Instituto de Biología Molecular de Barcelona, Consejo Superior de Investigaciones Científicas, Barcelona, Spain

[2] Mechanobiology Institute, National University of Singapore, Singapore

[3] Institute for Bioengineering of Catalonia, Barcelona, Spain

[4] CIBER de Enfermedades Respiratorias (CIBERES), Madrid, Spain

[5] Facultat de Medicina i Ciencies de la Salut, Universitat de Barcelona, Barcelona, Spain

[6] Laboratori de Càlcul Numèric (LaCàN), Universitat Politècnica de Catalunya, Barcelona, Spain

[7] Centre Internacional de Mètodes Numèrics en Enginyeria (CIMNE), 08034 Barcelona, Spain

[8] Institut de Matemàtiques de la Universitat Politècnica de Catalunya – BarcelonaTech (IMTech), Barcelona, Spain

[9] Institute of Molecular and Cell Biology, A*Star, Singapore

[10] Warwick Medical School, University of Warwick, Coventry, United Kingdom

[*] For correspondence embbmc@ibmb.csic.es, timothy.saunders@warwick.ac.uk, j.munoz@upc.edu

[#] Present address: A.S. Princeton University, USA. S.T. CNRS, Aix-Marseille Université, France.

[§] Lead Contact: Enrique Martin-Blanco, embbmc@ibmb.csic.es

## Summary

During development, organs reach precise shapes and sizes. Organ morphology is not always obtained through growth; a classic counterexample is condensation of the nervous system during *Drosophila* embryogenesis. The mechanics underlying such condensation remain poorly understood. Here, we characterize the condensation of the embryonic ventral nerve cord (VNC), at both subcellular and tissue scales. This analysis reveals that condensation is not a unidirectional continuous process, but instead occurs through oscillatory contractions. The VNC mechanical properties spatially and temporally vary, and forces along its longitudinal axis are spatially heterogeneous. We demonstrate that the process of VNC condensation is dependent on the coordinated mechanical activities of neurons and glia. These outcomes are consistent with a viscoelastic model of condensation, which incorporates time delays and effective frictional interactions. In summary, we have defined the progressive mechanics driving VNC condensation, providing insights into how a highly viscous tissue can autonomously change shape and size.

42

43 “What utilitarian goal has nature pursued in forcing nervous system differentiation to
44 these lengths? ..... The refinement and enhancement of reflex activity, which
45 protects the life of both the individual and the species” (Cajal, 1899).

46

47

48 **INTRODUCTION**

49 Morphogenesis proceeds as a result of changes in cells proliferation, adhesion,
50 differentiation and survival, and it is also the subject of mechanical inputs (Heisenberg
51 and Bellaïche, 2013; Hogan, 1999; Weber et al., 2011; Zhang and Labouesse, 2012).
52 Further, during ontogenesis, all organs develop in synchrony to reach physiological
53 optimization (Oliveira et al., 2014). In this scenario, how mechanics influences the final
54 shape or size of an organ remains far from clear (Heisenberg and Bellaïche, 2013; LeGoff
55 and Lecuit, 2015; Saunders and Ingham, 2019). A critical issue is that mechanical
56 processes must be highly coordinated, while also accounting for geometric and scaling
57 constraints (Amourda and Saunders, 2017).

58 Biological tissues display both elastic and viscous properties and are, in many cases,
59 mechanically heterogeneous both in space and time (Serwane et al., 2017). They are
60 constituted by active materials, and so standard equilibrium biophysical approaches are
61 often insufficient to describe their behaviors. Tissues material properties are thus key for
62 the development of the organism (Mammoto and Ingber, 2010; Miller and Davidson,
63 2013; Mongera et al., 2018). Yet, understanding how the material properties of tissues
64 impact the building and shaping of organs during development remains an open question.

65 Precise tissue organization is especially relevant when considering the functional
66 complexity of the Central Nervous System (CNS) (Redies and Puelles, 2001). The
67 complex architecture of the mature CNS is achieved through a well-known sequence of
68 cellular events (Roig-Puiggros et al., 2020; Tessier-Lavigne and Goodman, 1996). At the
69 local level, tension forces contribute to the formation and maintenance of active synapses
70 and the stabilization of neurites (Anava et al., 2009; Kilinc, 2018). They also influence
71 the shortening of neuronal processes, thus contributing to circuitry compactness (Franze,
72 2013). However, it is unknown which mechanical processes, at the tissue-scale, are

involved in the spatial organization of neural architecture.

Here we fill this knowledge gap by determining how mechanical forces translate into tissue level sculpting of the entire *Drosophila* embryonic ventral nerve cord (VNC) during its condensation. The embryonic CNS is built stepwise by neuroblasts that delaminate from the neurectoderm in an invariant pattern, generating a diverse population of neurons and glia (Hartenstein and Wodarz, 2013). Neurons are unipolar and project their axons towards the neuropil. Cohesive axon bundles travel together and branch in the same or closely adjacent neuropil compartments, creating stereotyped segmental structures (Landgraf et al., 2003; Technau, 2008). Axon tracts include three longitudinal connectives that pioneer the neuropil of the VNC, and transverse pioneer commissures establishing contralateral connections (Lin et al., 1994). Neurons are supported by a complex scaffold of glia, which builds a meshwork of cortex processes required for stabilizing neurons' positions (Beckervordersandforth et al., 2008). Macroscopically, the VNC exhibits a dramatic late shortening that further progresses in larval stages (Campos-Ortega and Hartenstein, 1985; Olofsson and Page, 2005; Page and Olofsson, 2008). It is worth noting that changes in embryo length do not substantially alter VNC condensation (Tiwari et al., 2021). From an architectural viewpoint, the mechanisms modulating how the CNS gets shaped and how its composing elements are brought together into a mechanically stable functional structure are unknown.

To analyze the VNC condensation dynamics across scales, we used four-dimensional confocal and light-sheet microscopy along with advanced image analysis. Velocity and strain maps revealed a complex morphogenetic kinematic, comprising alternate active and passive periods. Condensation, during the active phases, proceeds centripetally from both ends of the VNC and exhibits local oscillatory behavior. Further, spatial and temporal quantifications of material stiffness showed that the VNC displays a correlative, segmentally iterated, tensional landscape and stereotyped material stiffness inhomogeneities. We built a viscoelastic model and revealed that the periodic oscillations are consistent with the different viscous and elastic mechanical behaviors observed during tissue condensation. The combined experimental and theory results show that large-scale mechanical forces are essential for condensing and shaping the VNC. Its final shape depends on the concerted actions of neurons and glia through the dynamic modulation of their cytoskeleton. Overall, this work reveals that the nervous system behaves as a solid

viscoelastic tissue and that its biomechanical properties are key, in concurrence with a complex series of coordinated cellular actions, for its morphogenesis.

## RESULTS

### VNC cytoarchitecture

The structural organization of the embryonic VNC has been described in detail (Landgraf et al., 2003; Sanchez-Soriano et al., 2007; Zlatic et al., 2009). The axonal scaffold links repeated neuromere units and displays iterated transversal commissures and longitudinal tracts. Almost every neuron has been mapped and their lineages identified. To characterize the mechanical properties of the VNC, we first monitored the allocation of cell bodies and the distribution of cytoskeletal components.

We performed a cross-correlation analysis, employing the pan-axonal marker acetylated tubulin, to define the 3D organization of the VNC axonal network. This study revealed a pattern of axonal assemblies segmentally iterated along the anterior posterior (AP) axis, which could serve as anchoring architectural nodes (**Figure S1A** and **Movie S1**). We also found that neuronal cell bodies, from early stages, arrange along the AP axis in a periodic, contralaterally symmetric, segmental pattern, with most cells accumulating at the VNC ventral side (**Figure S2A-C**). This segmental periodicity is lost as the 3D topology consolidates.

The stereotyped architecture of the VNC (cell density and axonal scaffold) associates to a discrete mesoscopic distribution of cytoskeletal components. Microtubules uniformly distribute along all axonal protrusions, while Non-Muscle Myosin (NMM - Myosin II) and Actin (Phalloidin) show distinct distributions (**Figure S1B-C** and **Movie S1**). Actin periodically accumulates at intracommissural areas (and at the nodes) in each segment and Myosin II builds up along contralateral single-cell domains at the dorsomedial edge of the neuropile. Both, also, decorate longitudinal components.

### VNC condensation dynamics

To understand *Drosophila* VNC condensation mechanics, we characterized its progression *in vivo*, from the initiation of germ band retraction to larval hatching. Midway through embryogenesis, the VNC undergoes a dramatic compaction along the AP axis, shortening from over 700 to less than 250 μm (**Figure S2D** and **Movie S2**). This process depends on different cellular events: the remodeling of the extracellular matrix (ECM) by hemocytes; the cytoskeletal dynamics of glia and neurons; and regulated apoptosis (Evans et al., 2010; Olofsson and Page, 2005; Page and Olofsson, 2008). We live-imaged Fasciclin 2 (Fas2)-GFP embryos (Buszczak et al., 2007) by confocal microscopy and embryos expressing the nuclear marker Histone2A-mCherry by light-sheet microscopy (Krzic et al., 2012). Importantly, VNC 3D morphology reconstruction, from stage 16 onwards, was facilitated by a custom-made image processing pipeline that "detwitched" embryos digitally, re-locating the VNC along the central midline, at each time-point, from *in toto* light-sheet images **(Figure 1A, Movie S2** and STAR Methods**)**.

We generated length and velocity profiles for the VNC throughout condensation **(Figure 1B)** that revealed that it proceeds in five dynamic steps. First, the VNC pulls back, in parallel to the retraction of the germ band, until its posterior end positions near the tip of the embryo (compaction phase 1 – CP1). The condensation speed follows that of the germ band (Lynch et al., 2013). Second, the VNC reaches an almost stationary phase by the end of germ band retraction (end of stage 13). This phase lasts up to the end of dorsal closure and head involution by late stage 15 (pausing phase 1 – PP1). Third, the VNC, uncouples from the epidermis, and actively contracts (compaction phase 2 – CP2). Fourth, condensation rests again (pausing phase 2 – PP2). Last, the VNC undergoes a final slow progressive compaction, concurrent with peristaltic embryo movements, up to the end of stage 17 (compaction phase 3 – CP3). Variability in VNC length between embryos is very small (<10%) except during CP1 (see also (Tiwari et al., 2021)), which highlights the robustness of the condensation process, structured in active and passive phases **(Figure 1B)**.

## VNC condensation is oscillatory

At its onset, VNC condensation passively follows the movements of the germ band. The successive phases of contraction are, on the other hand, active processes. We undertook an analysis of these late steps quantifying, using particle image velocimetry (PIV) (Vig

et al., 2016), the local velocities along the whole length of the VNC (phases CP2, PP2 and CP3) **(Figure 1C**, **Movie S2)**. Remarkably, we found that, both during the CP2 and CP3 phases, condensation is oscillatory, with contractile periods of around 30 minutes. The frequency of the oscillations is quite regular, while their amplitude varies. Oscillations with opposing directionalities are present at the anterior and, prominently, at the posterior of the VNC **(Figure 1C)**. They lead to the bidirectional convergence of the VNC towards a central stationary domain between the third thoracic and the first abdominal segments (**Figure 1D** and **Movie S2**).

We conclude that the active periods of VNC condensation are not monotonic. Tissue-scale oscillations suggest a complex spatiotemporal mechanical coordination across the whole tissue. We hypothesize that the dynamic combinatorial activities of the glia and neurons lead to this complex tissue-scale behavior.

**Material properties of the VNC vary both spatially and temporally**

The complexity of VNC condensation kinematics hints to potential spatiotemporal changes in its material properties. To evaluate tissue stiffness, we used Atomic Force Microscopy (AFM). The elastic Young's modulus (E), a stiffness proxy, was measured segment-to-segment at the midline and at lateral cortex positions of stage 14 and late stage 16 embryos (**Figure 2A-C** and STAR Methods).

At stage 14 of embryogenesis (PP1), E was 0.08 ± 0.01 KPa (mean ± SD, n=15) in the midline, and 0.06 ± 0.01 KPa in the lateral regions (abdominal segments 1 to 5) **(Figure 2B)**. No statistical differences were found either between midline and lateral positions or along the AP axis ($p > 0.05$). At late stage 16 (CP2), the midline stiffness increased significantly when compared to the lateral cortex (0.17 ± 0.03 KPa vs 0.06 ± 0.02 KPa (n=15) ($p < 10^{-3}$). The central domain of the embryonic VNC, where most axons bundle, becomes more rigid than the lateral domains, where the somata are predominantly located. We also found that stiffness decreased towards the most posterior segments (**Figure 2C**; see also **Figure S3**).

In summary, the *Drosophila* embryonic VNC is extremely soft, consistent with previous measurements in neural tissues from different organisms (Spedden and Staii, 2013). Further, our results indicate that the neural tissue stiffens with time in an axially graded

fashion, as also observed in neural crest morphogenesis (Barriga et al., 2018; Shellard and Mayor, 2021).

## The tensional landscape of the VNC is temporally and spatially patterned

To infer large tissue scale forces, we first measured local strain rates. Strain rates measure how rapidly neighboring regions move relative to each other (Petridou and Heisenberg, 2019). They determine the resulting tissue stresses, which also depend on the viscoelastic tissue properties; its bulk viscosity and the local shear modulus (STAR Methods). The strain rate maps reveal that tissue deformations get restricted to specific subdomains of the VNC (**Figure 2D** and **Movie S2**). At the active CP2 and CP3 phases, the strain rates display alternating positive and negative values along the AP axis. The strain rate has a marked change in magnitude immediately after the second pause phase, slowly tending back towards zero. Distinct strain rate domains appear to correspond to iterative contractile regions repeated along the VNC. These regions map to the space between the posterior commissure of one neuromere and the anterior commissure of the next (intercommissural) **(Figure 2E)**.

Together, the strain rates and AFM data suggest that the VNC is mechanically organized in repeated units, and its mechanical properties are temporally modulated. To evaluate these propositions, we studied the VNC response to mechanical perturbation. We utilized laser microsurgery to sever the VNC at specific times and positions (**Figure 3A**, **Figure S4A** and STAR Methods). Cutting transversally to the AP axis in the intercommisural domains of abdominal neuromeres of stage 11-14 embryos, resulted in a faster isotropic recoil than in intracommissural regions (**Figure 3B**, **Figure S4B** and **Movie S3**). Thus, early (PP1), the intercomissural domains appear to be under significantly higher tension than the intracommissural. By contrast, tissue recoil during late condensation (CP2/PP2 - stages 16-17), was lost **(Figure 3C)**. Importantly, severing of a single intercommissural space does not affect the condensation of adjacent neuromeres that continue to condense as independent units (**Figure 3D** and **Movie S3**).

Laser cuts also enable by analyzing the recoil rate (see STAR Methods) an approximate characterization of the viscoelastic properties of the VNC. By severing the intercommissural domains at different time points we found a strong reduction of contractility and viscosity as the VNC condenses **(Figure 3E)**. Though we cannot

discount possible differences between the inter- and intracommissural domains, such variations in viscosity are likely negligible as their tissue composition is equivalent.

We next matched the iterated architectural organization of the VNC and its biophysical properties (stiffness and viscosity) and found they spatially correlate with the distribution of cytoskeletal components (actin and Myosin II) (**Figure S1**). This suggests that the dynamics of the actomyosin cytoskeleton could be crucial in modulating VNC's viscoelastic properties and condensation progression.

Last, to evaluate stress patterns along the VNC, we constructed a three-dimensional Finite Element (FE) model. We mapped the measured velocity field onto this model and reconstructed the strain and stress fields (**Figure 3F**, **Figure S4C-D**, **Movie S4** and STAR Methods). The evolution of the stress profiles along the AP-axis and the superposition of the stress minima (compression) onto the phase contrast kymographs, confirmed that maximum compression occurs at the intracommissural domains. Further, the active stress increased over time in the intercommissures **(Figure S4E)** pointing to a potential scenario in which the distribution of tension reflects the spaced contractions of the tissue. Segments contract as units directing condensation progression.

**Oscillations are an emergent property of a viscoelastic tissue**

The contraction of the intercommissural domains in between neuromeres explains the condensation of the VNC, but how do they coordinate? Can this coordination explain the origin of the global oscillations? To tackle these problems, we developed a one-dimensional rheological model that incorporates the viscoelastic properties of the VNC along with a delayed active contractility. At a particular time, *t*, the VNC is taken to have a rest length, *L(t)*. This internal variable depends on time, as the system gradually condenses. We define $\Delta L(t)=l(t)-L(t)$ as the difference in VNC length at time *t* from its rest length. The change in the rest length as a function of time would be

$$\frac{dL(t)}{dt} = \gamma \Delta L(t - \delta t) \qquad \text{Eq. (1)}$$

where $\gamma$ is the remodelling rate, which measures the rate at which the tissue adapts its rest length and $\delta t$ represents the time delay between the current strain measure $\Delta L$ and the active remodeling of the VNC through its rest-length $L$.

The VNC it is connected early to the underlying epithelia and late by intersegmental and segmental nerves to the developing muscles and peripheral sensory organs. Further, it is surrounded by the neural lamella (Meyer et al., 2014). We then incorporated potential effects of surrounding tissues adding a frictional term proportional to the apparent VNC length rate *dl/dt,*

$$-\eta \frac{dl(t)}{dt} = k_1 \cdot \Delta l(t) + k_2 \cdot \Delta L(t) \qquad \text{Eq. (2)}$$

where $\eta$ is the friction coefficient, $k_1$ is the purely elastic component of the VNC, $\Delta l(t)=l(t)-l_0$, where $l_0$ is the characteristic elastic length scale, and $k_2$ represents the stiffness of the viscoelastic component of the VNC, with a dynamic rest-length $L(t)$. (**Figure 4A**). The combination of Eqs. (1) and (2) yields a viscoelastic model with a delayed viscous response, which has the ability to exhibit oscillatory behavior (Dawi and Munoz, 2021).

We utilized our above quantitative measurements to constrain our model parameters. The time delay was chosen such that similar frequencies to the experimental ones were obtained *in silico*, when considering the measured stiffness and viscosity. In fact, the period of the oscillation is proportional to the delay (Muñoz et al., 2018), which allows us to define the delay value corresponding to the observed oscillation period. Our chosen values of viscosity and stiffness matched the characteristic time of the tissue, between 5 and 15 s, which in our model is equivalent to the factor $\eta/k_2 \sim 8$ s (see **Figure 4A**).

Similar rest-length models have been used in the context of embryogenesis (Cavanaugh et al., 2020; Doubrovinski et al., 2017; Sumi et al., 2018), epithelia remodeling (Clement et al., 2017; Staddon et al., 2019) and stress relaxation of monolayers (Khalilgharibi et al., 2019). The stability of such models with the delay rheology in Eq. (1) considering environmental viscous effects has only recently been analyzed (Dawi and Munoz, 2021).

Eqs. (1)-(2) form a system of Delay Differential Equations that can be analyzed through their characteristic equation (Erneux, 2009; Stépán, 1989) or numerically. Depending on the parameters $\eta$, $\gamma$, $\delta t$, $k_1$ or $k_2$, the apparent length $l(t)$ can exhibit either a stable regime (with no oscillations or oscillations showing a diminishing amplitude) or unstable oscillations (with increasing amplitude). The phase diagram in **Figure 4B** shows that decreasing values of $k_2$ render the system unstable, while decreasing values of viscosity $\eta$ and $\gamma$ render more stable oscillations. These results are consistent with the stabilization

of the VNC as its stiffness increases **(Figure 2B-C)** and its viscosity is progressively reduced **(Figure 3E)**. The kymograph, in **Figure 4C,** shows an example of the stable oscillatory regime (see **Figure S5A-D** for other scenarios). Overall, our reduced one-dimensional model can explain the emergence of periodic contractions as a consequence of time delays conveyed by the material properties of the VNC and the effective friction between the neural cortex and the surface glia. As the VNC stiffens during development, these oscillations are stabilized, ensuring the condensation of the VNC.

As described, the results above are based, assuming some simplifications, on parameters values matching the experimental data. We then tested how robust our model was to parameter variation. To analyze the sensitivity of the VNC condensation to changes in the viscoelastic and regulatory parameters ($\gamma$, $k_1$, $k_2$, $\eta$ and $\delta t$) and to define the range compatible with an oscillatory regime, we performed *in silico* simulations, jointly analyzing changes in amplitude and frequency of oscillations and the effective condensation (**Figure 4D (i-v)**). We found that viscous values under $15*k_2$ or a time delay below ~15 s prevent the appearance of oscillations, or, at least, strongly reduce their amplitude, in the final stages of condensation. The frequency of the oscillations is in general unaffected, except for the delay $\delta t$, where frequencies increase upon reduction of the time-lag.

In our simulations, we found that both condensation and tissue oscillation were sensitive to $\gamma$ (which represents the effective rate of cell remodeling to contractile forces and is probably dependent on actomyosin dynamics). A reduction of $\gamma$ by only 10% led both to condensation defects and alterations of oscillatory patterns (**Figure 4D (i)**). The sensitivity of the model to changes in $\gamma$ is consistent with our observations above on the distribution of actomyosin cytoskeleton components. These results suggest that actomyosin activity plays a significant role on the mechanics of VNC condensation.

## VNC condensation requires significant mechanical contribution from glia

Can differences in material properties and emergent oscillations be connected to cell behaviors? Considering the complex mechanics of VNC condensation, we next asked if neurons or glia - play a mechanically active part in modulating tissue scale behavior and, if they do, we aimed to determine their effects on the VNC material properties. We genetically ablated either neurons or glia by overexpressing the proapoptotic gene Grim

(Chen et al., 1996) employing the pan-neural Elav-Gal4 and the glia Repo-Gal4 drivers **(Figure 5A-D)**.

Excessive neuronal cell death heavily distorted the organization of the axonal scaffold **(Figure 5A)**, and, to a lesser extent, VNC condensation **(Figure S6B)**. Yet, apoptosis is a slow process and, possibly, late neurons, born halfway during condensation, could escape death. Neuron elimination was not fully penetrant and many ELAV positive cells were negative for Dcp1 (dying cells marker) (**Figure S6A**). No spurious apoptosis was detected, although glia mis-positioned, probably in response to steric constrains resulting from alterations in axonal morphology **(Figure 5B)**.

Expressing Grim in glia promoted slight alterations in the 3D axonal scaffold **(Figure 5C)**. Contrary to neurons, most of the glia was removed **(Figure 5D)**, which resulted in a strong failure of the condensation process **(Figure S6B)**. Loss of glia also altered the VNC shape (**Figure 5E** and **Movie S5**). We further studied glia depletion employing light sheet microscopy (**Figure S6C** and **Movie S5**) and found that in its absence, condensation arrests at the last contraction phase (CP3) **(Figure 5F)**. PIV analyses revealed a substantial reduction of VNC strain rates and the loss of contractile oscillations **(Figure S6D)**.

Last, we explored by AFM the impact of neurons or glia on the VNC material properties. AFM measurements were performed at the stationary PP1 (stage 14, **Figure 5G**) and active condensation CP2 phases (stage 16, **Figure 5H**). Before active contraction, VNC rigidity slightly decreased at the midline after neuron ablation but it was not affected by glia depletion. On the contrary, during the active CP2 phase, significant softening upon glia removal was observed, both at the midline and at lateral positions, while neuronal ablation had no effect (**Figure 5H**).

From the stability diagram of our rheological model (**Figure 4B),** we infer that, as the VNC condensation progresses, the viscoelastic parameters, rigidities $k_1$ and $k_2$ and viscosity $\eta$, proceed from a sector where oscillations tend to increase to a sector where oscillations tend to diminish. Further, the sensitivity diagrams (**Figure 4D (ii-iv)**) indicate that an increase in rigidity causes a resistance to condensation that results in larger final VNC relative length. This is in accord with the slowdown of shortening (**Figure 1B**) and increase of stiffening (**Figure 2B-C**) observed as condensation progresses.

353 The sensitivity analyses do not predict a shortening of the VNC relative length upon
354 drastic reduction in rigidity (**Figure 4D (ii-iii)**), opposite to what it is found after glia
355 removal (**Figures 5G-H**). In this case, however, softening affects oscillations, as shown
356 on the stability diagram (**Figure 4B**), and this will eventually disrupt condensation
357 (**Figure 5F**). On the other hand, when rigidity is only mildly disturbed, as occurs after
358 neuronal ablation (**Figures 5G-H**), the rheological model predicts that the oscillatory
359 response would remain largely unaffected as it happens.

360 In summary, both glia and neurons contribute to the active contraction of the VNC and
361 modulate its material properties. However, while glia has a major contribution on both of
362 these aspects, the impact of neurons appears to be more subtle; they mainly influence the
363 structural organization of the neuropile and not VNC material properties.

364

365 **Myosin-mediated contractility in neurons and glia is required for VNC**
366 **condensation**

367 VNC condensation is an active process demanding mechanical efforts. To evaluate the
368 mechanical impact that the active cytoskeleton may have in condensation, we analyzed
369 actomyosin contractility in both neurons and glia.

370 We found that Zipper (Zip) (Non-Muscle Myosin II heavy chain) knockdown led to
371 distinct spatiotemporal alterations on VNC condensation dynamics (**Figure 6** and **Movie**
372 **S6**). Abolishing neuronal contractility by pan-neural expression of a RNAi transgene
373 (Elav-Gal4/UAS-Zip RNAi) resulted in major defects in the structural scaffold and in
374 condensation failure from CP2 onwards **(Figure 6D)** without any increment in cell death
375 (**Figure 6A** and **Figure S7A**). Interestingly, although no condensation progression was
376 detected, segmentally iterated displacements and strain patterns still occurred.

377 Interference on Zip expression in glia (Repo-Gal4/UAS-Zip RNAi) resulted in cessation
378 of condensation at the PP2 phase **(Figure S7A)**. Glia looked smaller and failed to migrate
379 properly and the neuronal longitudinal axonal tracts were misplaced closer to the midline
380 **(Figure 6B)**. On the contrary to neurons, depletion of Zip in glia resulted in a strong
381 disruption of iterative strain profiles **(Figure 6E)**.

382 The aberrant strain patterns observed after Myosin II depletion in glia suggest that in this
383 condition the oscillatory regime may also be affected. We evaluated the oscillatory

patterns upon mild and strong interference in Zip expression in glia (Repo-Gal4/UAS-Zip RNAi embryos at the CP2 phase, taking advantage of the temperature sensitivity of the Gal4 transactivator (weak at 18ºC and strong at 29 ºC). Importantly, we found that the developing temperature affects oscillations. In representative control animals, both periodicity and amplitude were larger (~53 vs. ~48 minutes and ~7 vs. ~4 μm) when developing at low, than at high temperature. Upon Zip RNAi overexpression, the periodicity of the oscillations with respect to control animals was not affected (~54 and ~45.5 minutes at 18 and 29ºC respectively) while the amplitude was strongly reduced (~4 and ~3 μm at 18 and 29ºC respectively). Thus, the oscillations' amplitude correlates with the degree of contractility inhibition.

Concerning the rheological model (**Figure 4A),** the description of the VNC condensation process in terms of viscoelastic and regulatory parameters does not distinguish, in principle, between neurons and glia. Yet, reducing $\gamma$ in the phase space plots (**Figure S5F and H**) results in a severe condensation defect in which the strain pattern is sustained, which mimics the observed when Myosin II is downregulated in neurons. On the contrary, upon blocking contractility in glia, no compression of intercommissural regions occurs and the strain rate pattern is lost (**Figure 7A** and **7B** and **Movie S7**). These observations suggest that within the model framework, neurons are primarily associated to condensation regulatory parameters (remodeling rate $\gamma$ and delay $\delta t$), which control the oscillatory behavior. Conversely, glia is associated with the material properties (stiffness $k_1$, $k_2$ and viscosity $\eta$) that enable condensation. Specifically, $\eta$ likely relates to the friction between neurons and the glia/ECM. These roles are, most probably, not completely uncoupled since ablation of neurons has also minor effects on rigidity (see **Figure 5G**), while Myosin II depletion on glia induces a relevant decrease of oscillatory amplitude.

Altogether, our data support a model in which neuronal contractile capability, at all stages, has a permissive regulatory role but it is not sufficient for tissue compaction. Likely, in the absence of Myosin II, neurons resist the compression forces generated by the surrounding glia. The glia otherwise exerts an external compressive force at the VNC surface, which is spatiotemporally regulated and exploits the segmentally iterated architectural organization of the neuronal network to accommodate the periodic tensional pattern of the VNC into oscillatory condensation events **(Figure 7C-E)**.

## DISCUSSION

In discussing the spatial design of the nervous system, we have to consider some specific features, the organism symmetry, the spatial configuration of its sensorimotor machinery and the need to create a design that serves functional integration (Bullmore and Sporns, 2012; Swanson, 2007). The condensation of the VNC, within the global CNS developmental plan, respects these traits. The VNC sustains iterated axonal connections to all segments' muscles and sensory organs.

Multiple cellular events play key roles in VNC condensation, in particular interactions between neurons and glia, and apoptosis (Meyer et al., 2014; Olofsson and Page, 2005; Page and Olofsson, 2008). Several intrinsic and extrinsic events are also ultimately linked: the deposition of the ECM; dorsal closure and head involution or midgut' closure. While some signaling pathways have been shown to participate in VNC condensation, we do not understand the events leading to its mechanical control. Information is also missing on the cellular rearrangements occurring within the packed 3D structure of the VNC. Neuronal cell bodies are essentially round and do not deform or intercalate during condensation. The more planar glia decorating the surface of the VNC does not suffer axial compression; instead, it remodels its shape adapting to the VNC contour changes. The role of ECM remodeling, which has been long recognized as an important element during condensation (Matsubayashi et al., 2020; Meyer et al., 2014; Olofsson and Page, 2005; Pastor-Pareja and Xu, 2011) remains undefined.

### The condensation of the VNC is oscillatory and serves specific purposes

Condensation is a common morphogenetic event (Hall and Miyake, 2000) affecting multiple tissues. It plays an important role at the primary steps of organogenesis (*e.g.* cartilage, bone, muscle and tendon) (DeLise et al., 2000) and in shaping neural ganglia, both in arthropods (Bullock and Horridge, 1965) and vertebrates (Stark et al., 1997). In most of these cases, cells get together by migratory accretion or intercalary growth (Christley et al., 2007; Frenz et al., 1989; Singh and Schwarzbauer, 2012). The *Drosophila* VNC condensation follows specific allometric constraints to reach full

functional competence (Karkali et al., 2020). This is achieved through sequential active and passive stages and oscillatory behavior. This complexity has not been observed before in any equivalent process.

Oscillations may arise on epithelia with planarly-connected cells (Peyret et al., 2019) and they can also be anticipated in a tissue structurally segmented or with repeated alternations of stiffer/softer, viscous/less viscous domains. Yet, there are examples of segmentally repeated tissues that do not oscillate as they change shape (e.g. *Drosophila* germ band extension (Bertet et al., 2004), and examples of tissues not segmentally iterated that do oscillate (e.g. *Drosophila* amnioserosa (Solon et al., 2009)). For the VNC, oscillations, *a priori,* were not expected.

Are VNC oscillations linked to (or an aftermath of) the stereotyped alternating organization of the VNC? The reproducibility and robustness of the oscillatory regime appears to suggest so. However, interfering in contractility in glia or neurons differentially affects the strain rates pattern and condensation regimes (**Figure 6D-E**), without affecting the VNC alternating architectural organization. In conclusion, the oscillatory regime does not appear to be an unavoidable side-effect of the organization of the tissue and to be biologically relevant.

**Oscillations are an emergent property of the viscoelastic character of the VNC**

The condensation of a tissue is the result of the spatially-patterned dynamics of its components. The directionality and magnitude of such patterning are critical for changes in the tissue's fine structure and properties (Li et al., 2017; Shyer et al., 2017).

During condensation the VNC tissue material properties and tensional mechanics undergo progressive changes (**Figures 2** and **3**). The embryonic VNC is very soft (as other neural tissues (Franze et al., 2013)) and its stiffness is neither constant, nor homogeneous. Additionally, an iterated tensional pattern rises and falls following segmental structural landmarks along the AP axis. Overtime, condensation leads to a rigid structural configuration in equilibrium, in which tensional differences are smoothed out.

Up to now, the lack of suitable biophysical models has limited the study of the mechanics during condensation. There are multiple models that can mimic oscillatory responses, either through combining reaction-convection terms (Notbohm et al., 2016) or oscillatory

polarization and alignment (Petrolli et al., 2019; Peyret et al., 2019). Here, we developed a simple one-dimensional viscoelastic model FE model to infer strain and stress maps. This not just simulates the periodic oscillations of the VNC, but it predicts the different oscillatory regimes associated to the changes of viscous and elastic mechanical properties observed **(Figure 4)**. Fitting the rigidity values retrieved from AFM measurements, it reveals oscillations in the absence of any external inputs. Oscillations arise as a consequence of the delayed remodeling of the tissue with respect to the compressing forces. The oscillatory regime of VNC condensation thus depends on its material properties and effective frictional interactions with its surroundings. The fact that increasing viscosity destabilizes oscillatory behavior can be interpreted by an additional delay induced by frictional forces.

From the modeling point of view, the addition of a time delay is expected to induce oscillations in a dynamical system. However, time delays are not sufficient and, in our model, no oscillations are obtained below threshold values of $\delta t$. We note that in the field of biological clocks there has been extensive analysis of oscillatory models (Le Novère, 2015; Negrete and Oates, 2021; Novák and Tyson, 2008), and including time delays does not trivially make a system oscillate (Muñoz et al., 2018).

In determining oscillatory robustness, our rheological model predicts that viscosity and time delay are key factors (**Figure S5E-H** and **Figure 4D**). Double sensitivity analyses of model parameters (**Figure S5E-H),** with respect to relative final length (condensation), also revealed the non-linearity of this length relative to elastic stiffness. Indeed, an increase in rigidity opposes the active contractility of the VNC, while the observed decrease of viscosity over time, in accord with the sensitivity analyses (**Figure 4D (iv)**), may be responsible of the progressive slowdown of condensation (**Figure 1B**).

## VNC condensation requires the mechanical contribution of glia and neurons

VNC condensation bears mechanical similarities to the compaction of accordion bellows, in which each pleat corresponds to a neuromere unit. Though each “pleat” in the VNC can contract autonomously, they are temporally and directionally coordinated across a long-range by force continuity and balance. This results in oscillatory regimes extending throughout the VNC. We have found that this long-range continuity is created by a precise coordination of the contractile activities of neurons and glia.

In the VNC around 60 glial cells are identified per neuromere (Ito et al., 1995). Amongst them, the Subperineurial Glia (SPG) is responsible for establishing the Blood Brain Barrier (BBB) (Schwabe et al., 2017). Two pieces of evidences point to the key role of glia in VNC condensation: the ablation of hemocytes, which causes severe defects in SPG morphology (Martinek et al., 2008; Olofsson and Page, 2005), and the interference with Rac1 or Heartless signaling in the lateral glia (Olofsson and Page, 2005), both block condensation progression. The mechanical contribution of glia to VNC condensation may be linked to its participation in casting the BBB. Yet, our evaluation of the mechanical consequences of glia removal indicates that it does not just act as a barrier, but it also operates as a "compression sock", wrapping the VNC cortex and providing rigidity (**Figures 6** and **7**). In its absence, condensation is irregular, shows a substantial reduction in its strain rates, and lacks contractile oscillations. We found that interfering in the contractile capability of the SPGs was sufficient to phenocopy pan-glial myosin activity depletion, both in terms of condensation **(Figure S7A)** and axon network organization (**Figure S7B**). The capability of glia to compact is strongly dependent on actomyosin contractility, and it is mainly allocated to the SPGs.

Each abdominal hemisegment of the VNC comprises around 400 neurons, whose axons arrange into segmental and intersegmental nerves and longitudinal connectives that constitute a potential force-generating source. Consistently, in some metamorphic insects, the longitudinal connectives loop during condensation (Pipa, 1973). We also found that the domains in-between neuromeres subside as condensation progresses. These domains are under tensional stress at early stages, relaxing as condensation proceeds. Thus, the axonal network appears to resist rather than to promote AP compaction. Although, ablation of neurons only marginally affects condensation, when their contractile capability was abolished, VNC condensation failed without significantly altering the strain patterns. Thus, neurons are not playing a purely passive role (**Figures 6** and **7**).

Overall, this work reveals that the viscoelastic and biomechanical properties of the nervous system, in concurrence with a complex series of coordinated cellular actions, are important for its morphogenesis. The generation of force patterns, and the ultimate acquisition of the VNC final shape, can be assigned to the concerted actions of neurons and glia through the dynamic modulation of their cytoskeleton. The neuronal contractile capability is secondary to the glial compacting power, but necessary to direct VNC condensation along the AP axis **(Figure 7C-E)**.

Finally, if we assume that VNC condensation is a way to respond to evolutionary pressure for functional optimization, we speculate that the segregation and coordination of mechanical activities between emergent neurons and glia is a key factor for natural selection.

## Limitations

VNC condensation oscillatory progression seems to depend on tissue mechanics and a time delayed response of adjacent elements. We assume that time delay is conveyed by the material properties of the VNC and the effective friction between the neural cortex and the surface glia, but this must be explored further. Indeed, the potential role of the ECM in altering the material/mechanical properties of the VNC or in the oscillatory behavior of the condensation process remains to be determined.

There are two other important points to be clarified in relation to the process of VNC condensation. First, condensation proceeds through active and passive stages. In particular, how it transits from the early passive phase, associated to germ band retraction, to the autonomous oscilatory active compaction, after dorsal closure, is unknown. We do not know either, how the bidirectional character of the condensation is regulated, how the anchor point is determined or how it works. All these issues could be related to the dynamic interactions of the VNC with adjacent tissues, such as the gut or the epidermis, which must be clarified.

## ACKNOWLEDGMENTS

We would like to thank C. Klämbt, N. Tolwinski and P. Tomancak for critical reading of the manuscript, E. Rebollo for her support at the Molecular Imaging Platform of the IBMB and S. Grill, MPI-CBG, for providing access to the laser ablation microscope.

KK and EMB are supported by grants BFU2017-82876-P of the Spanish Ministry of Science, Innovation and Universities (MICINN) and Fundación Ramon Areces to EMB. Work in the laboratory of TES (PT, AS and ST) was supported by a Singapore NRF Fellowship (2012NRF-NRFF001-094), an HFSP Young Investigator Grant (RGY0083/2016), MBI Core funding and start-up funding from the University of

Warwick. IJ and DN were supported by the grant DPI2017-83721-P (MICINN) and the Marie Skłodowska-Curie grant "Phys2BioMed" 812772. JJM is financially supported by the MICINN and by the Generalitat de Catalunya, under the grants DPI2020-116141GB-I00 and 2017 SGR 1278, respectively.

## AUTHOR CONTRIBUTIONS

Conceptualization, KK, TES, JJM, and EMB.; Methodology, DN; Investigation, KK, PT, AS, ST, I.J, TES, JJM. and EMB.; Writing – Original Draft, EMB; Writing – Review & Editing, KK, JJM, TES and EMB; Funding Acquisition, TES, JJM, DN and EMB; Resources, DN and TES; Supervision, TES, JJM and EMB.

## DECLARATION OF INTERESTS

The authors declare no competing interests.

## FIGURE LEGENDS

### Figure 1: Dynamics of VNC condensation

**A)** Snapshots at 2 min intervals from **Movie S2 (**multi-view light-sheet imaging of a live Histone 2Av-mCherry embryo, ventral view, late stage 17). mCherry marks all nuclei; raw data is shown on the left and "detwitched" images (blue masked) on the right. In all images, unless stated otherwise, anterior is to the left. Lines indicate the ventral midline. Scale bar 50 μm. **B)** Quantification of VNC length (**i**) and condensation speed (**ii**) as a function of time. Condensation (CP1, CP2 and CP3) and pause (PP1 and PP2) phases are masked in pale green and red, respectively. As a convention, t=0 corresponds to the onset of PP1, at the end of germ band retraction. Means (solid) and SD (dashed) are represented by red lines. Gray lines represent individual embryos (n=11). **C)** Condensation velocity dynamics. (**i**) Snapshot of a live Histone 2Av-mCherry embryo monitored by light-sheet

603 imaging, at stage 16. Scale bar 50 μm. (**ii**) Velocity kymograph derived from PIV analysis
604 (STAR Methods). Position=0 corresponds to the hinge between the brain lobes and the
605 VNC. Time axis (top to bottom) as in **(B)**. Color-coded positive (posterior-ward -
606 white/yellow) and negative (anterior-ward - black/blue) velocities (neutral - red). (**iii**)
607 Representation of velocity profiles (CP2, PP2 and CP3) with 5-minute resolution, along
608 the AP axis from the most anterior (darkest blue) to the most posterior (darkest red lines)
609 VNC positions. **D)** Kymograph along the VNC from a live embryo expressing Fas2-GFP.
610 (**i**) Ventral view from **Movie S4**, at stage 16. Scale bar 50 μm. (**ii**) Stage 16 embryonic
611 VNC, re-sliced over the Z-axis. (**iii**) Fluorescence intensity peaks landmark individual
612 segments (color coded as in **(C)**). Time and AP axis positions are as in **(B)** and **(C)**. (**iv**)
613 Kymograph of condensation, with arrows denoting condensation direction.

614

615 **Figure 2: Characterization of VNC material properties**

616 **A)** Representative images of flat dissected embryos at stages 14 and 16. VNC perimeter
617 (white) and midline (yellow) are highlighted. Anterior is to the top. Scale bar 50 μm. **B)**
618 Measured VNC stiffness (E) at early stages (13-14). Bars denote mean values (abdominal
619 segments A1 - A7). Mean stiffness was measured at the midline (blue) and at lateral
620 positions of the cortex (red). Dots and diamonds correspond to individual measurements.
621 **C)** as **(B)** but for older, stage 16-17, embryos. **D)** (**i**) Kymograph of VNC strain rates,
622 from **Figure 1C** (see STAR Methods). (**ii**) Representation of strain rates profiles (CP2,
623 PP2 and CP3) with 5-minute resolution, from most anterior (darkest blue line) to most
624 posterior (darkest red line) positions. (**iii**) Distribution of strains along the AP- axis for
625 all time points (earliest light to latest dark lines) during CP2 (green), PP2 (gray) and CP3
626 (green). **E)** Average size (and SD) of intra- and inter-commissural domains from early
627 (E) vs late (L) stage 15 and 16 and early (E), middle (M) and late (L) stage 17 embryos.
628 Data was collected from 7-10 measurements per time-point from two embryos.

629

630 **Figure 3: Laser microsurgery during condensation and tissue tension**

631 **A)** Representative images of stage 14 embryos, expressing alpha Tubulin-GFP, before
632 (top) and after (bottom) laser ablation. The yellow dashed line highlights the position of
633 the laser cut, while green (anterior) and red (posterior) arrows indicate tensile recoil
634 directionality **(Movie S3)**. Scale bar 10 μm. **B)** Post-ablation recoil velocity measured at

intercommissural (dark) and intracommissural (pale) domains, at stage 14 embryos. Bars represent mean recoil velocity of anteriorly (green) and posteriorly (red) retracting tissue. Individual measurements are denoted by yellow dots (intercommissural) and diamonds (intracommissural). * $p < 0.05$. **C)** Recoil velocity of anteriorly (green) and posteriorly (red) retracting domains after VNC ablation at different stages of embryonic development (n=12 embryos). **D)** (**i**) Tiled image of a stage 16 embryo expressing alpha Tubulin-GFP after laser cutting the intercommissural domain between the segments A1 and A2. The white arrow marks the direction of condensation. The anterior and posterior tips of the VNC and the abdominal segments (A1 to A8) are indicated (yellow). (**ii**) Snapshots, immediately post-ablation (masked blue), and 2 hours later (masked red), from **Movie S3**. Scale bar 20 μm. (**iii**) Superimposed intensity profiles of both time points. Black arrows indicate the magnitude of the anterior-ward displacement of individual segmental landmarks. **E)** Characteristic recoil time $\tau$ computed from the rate of recoil at the intercommissural domain. **F)** Kymograph of the VNC during condensation (Fas2-GFP). White curves correspond to fourth order polynomial fitting of the points of maximum compression as deduced from the viscoelastic FE model (STAR Methods). (See also **Figure S4D** and **Movie S3**).

**Figure 4: Rheological model of VNC condensation**

**A)** Scheme of one-dimensional rheological model including a viscoelastic term with variable rest-length $l$, stiffness $k_2$ and remodeling rate $\gamma$ (Eq. (1)). In parallel, carries an elastic component with stiffness $k_1$ and considers viscous contacts to the external environment, denoted by $\eta$. **B)** Phase diagram in the parameter space $k_2$ - $\eta$, showing that reduction of $\eta$ and increase of $k_2$ stabilizes the oscillatory behavior. St 14 and 17 characterize the transition from early to late condensation stages, with a stabilizing effect. **C)** Kymograph of numerical simulation showing the oscillatory behavior of strains as a function of time. **D)** Sensitivity of VNC shortening and oscillatory frequencies to main model parameters on (**i**) Remodeling rate, $\gamma$. (**ii**) Stiffness, $k_1$. (**iii**) Stiffness, $k_2$. (**iv**) Viscosity, $\eta$. (**v**) Time delay, $\delta t$. Shortening is measured as the relative final length, $l_{final}$ / $l_0$. The dotted blue line indicates the initial amplitude of the oscillations for the reference parameters ($\gamma$, $k_1$, $k_2$, $\eta$, $\delta t$) = (0.2, 0.01, 1.9, 15, 20), while the gray area represents the final amplitude for the analyzed values indicated on the horizontal axis. The green line

indicates the oscillations frequency as a function of the parameter values. Frequency is measured in $min^{-1}$ *10.

**Figure 5: Neurons and glia contribute to the architectural organization of the VNC and its condensation**

**A)** CNS Flat-preps of WT (top) and Elav-Gal4>UAS-Grim (bottom) embryos, at stage 16, immunostained for Fas2 (red) and Dcp1 (green). **B)** Embryos as in **(A)**, immunostained for Dcp1 (red) and Repo (green). **C)** CNS Flat-preps of WT (top) and Repo-Gal4:UAS-mCD8-GFP>UAS-Grim (bottom) embryos, at stage 16, immunostained for Fas2 (red) and GFP (green). **D)** Embryos as in **(C)**, immunostained for Dcp1 (red) and GFP (green). Yellow arrowheads point to the disrupted axonal network in **A** and **C.** Pink arrowhead points to misplaced or surviving glia in **B** and **D**. Scale bar 10 μm. **E)** Snapshots from time lapse recordings of WT (Top) and Repo-Gal4>UAS-Grim (bottom) embryos, in an alpha Tubulin-GFP background (ventral view –stage 17) **(Movie S8)**. Yellow arrowhead points to the VNC misshaped buckling. Scale bar 50 μm. AP axis orientation is indicated. **F)** Quantification of VNC length (*elav*:mCD8-GFP marker) as a function of developmental time in WT (red, n=11) and Repo-Gal4>UAS-Grim (blue, n=4) embryos. Solid and dashed lines show mean and SD values. **G)** VNC stiffness (E) measured by AFM at early stages 14, for WT, Elav-Gal4>UAS-Grim and Repo-Gal4>UAS-Grim embryos. Bars denote mean values at the ventral midline (blue) and at lateral cortex (red). *$p < 0.05$ , **$p < 10^{-2}$ and ***$p < 10^{-3}$. **H)** As **(G)** but for late stage 16 embryos.

**Figure 6: Active contractility in neurons and glia have distinct roles.**

**A)** Ventral and Dorsal 3D views of stage 16, WT (top) and Elav-Gal4>UAS-Zip-RNAi (bottom) embryos, immunostained for Fas2 (red) and Dcp1 (green). **B)** Ventral and Dorsal 3D views, as in **A**, of stage 16, WT (top) and Repo-Gal4:UAS-mCD8-GFP>UAS-Zip-RNAi (bottom) embryos, immunostained for Fas2 (red) and GFP (green). Yellow arrowheads point to the disrupted axonal network in **A-B**. Pink arrowheads point to misplaced glia. Scale bar 10 μm. **C-E)** Condensation dynamics in control **(C)**, Elav-Gal4>UAS-Zip-RNAi **(D)** and Repo-Gal4>UAS-Zip-RNAi **(E)** embryos **(Movie S7)**. (**i**) Snapshots of live embryos, expressing Fas2-GFP at stage 17. Yellow arrowheads point

to the posterior tip of the VNC in **D** and to the VNC misshaped buckling in **E**. Scale bar 50 μm. (**ii**) Representation of velocity profiles along the AP axis, from the most anterior (darkest blue) to the most posterior (darkest red line) VNC positions (as in **Figure 1C**). (**iii**) Kymograph of strain rates along the VNC (as in **Figure 2D**). Cyan marks point to strain oscillations.

**Figure 7: Neurons and Glia cooperatively contribute to the oscillatory behavior**

**A)** Snapshot from the 3D representation **(Movie S7)** of the 2D strain pattern of the VNC in WT animals. The 3D meshwork (top) is aligned to the corresponding raw image (bottom). **B)** Displacements and strains along the VNC in WT and in embryos with pan-neural (Elav-Gal4>UAS-Zip-RNAi) or pan-glial (Repo-Gal4>UAS-Zip-RNAi) Myosin II knockdown, at equivalent times [14 hours after egg laying (AEL) at 29ºC] **(**Snapshots from **Movie S7)**. **C)** Cartoon describing the condensation oscillatory regime during the CP2 and CP3 stages (at the level of the segments A4 and A7, data from **Movie S2** – see **Figure 1C**), highlighting the opposing displacements of thoracic (red) and abdominal (green) segments towards the central stationary domain. **D)** Cartoon representing the segmentally iterated intercommissural and intracommissural domains of the axonal network before (top) and after (bottom) condensation. Their mechanical properties (rigid or tensile) are shown. This representation depicts the first three abdominal segments actively contracting (green arrows). **E)** Cartoon presenting in 3D the VNC segmental axonal network (as in **D**) surrounded by the glial shell (SPGs), displaying centripetal and longitudinal contractile capability (blue arrows).

## STAR METHODS

## RESOURCE AVAILABILITY

### Lead Contact

Further information and requests for resources and reagents should be directed to and will be fulfilled by the lead contact, Enrique Martin-Blanco (embbmc@ibmb.csic.es).

## Materials and codes availability

This study did not generate new unique reagents.

All original code has been deposited at Github and is publicly available as of the date of publication.

# EXPERIMENTAL MODEL AND SUBJECT DETAILS

## *Drosophila* Stocks and Genetics

*Drosophila melanogaster* flies were grown on standard food at 25°C or 18°C, and experiments were performed at 25°C unless otherwise specified. *Drosophila melanogaster* stocks used in this study and associated references are listed in the **Key Resource Table**. Both female and male animals were used in all experiments.

All crosses were performed at room temperature and after 48 hours were shifted to different temperatures as the individual experiments required.

# METHODS DETAILS

## Sample Preparations for Immunodetection

*Drosophila* embryo dissections for generating flat preparations were performed according to (Landgraf et al., 1997). Briefly, flies maintained in apple juice-agar plates at 25ºC were synchronized by repetitive changes of the juice-agar plate, with a time interval of 2 hours. All embryos laid within this time window were aged for approximately 9 hours at 29ºC, or until reaching mid-stage 16 (3-part gut stage). At this point embryos were dechorionated with bleach for 1 min, poured into a mesh and rinsed extensively with water. For dissection, embryos were transferred with forceps on the surface of a small piece of double-sided tape, adhered on one of the sides of a poly-L-Lysine coated coverslip. After orienting the embryos dorsal side up and posterior end towards the center of the coverslip, the coverslip was flooded with saline (0.075 M Phosphate Buffer, pH 7.2). Using a pulled glass needle the embryos were manually de-vitellinized and dragged to the center of the coverslip, where they were attached to the coated glass with their ventral side down. An incision on the dorsal side of the embryo was performed using the

glass needle from the anterior to the posterior end of the embryo. The gut was removed by mouth suction and a blowing stream of saline was used to flatten their lateral epidermis.

**Immunohistochemistry**

Immunostaining of flat-prepped stage 16 *Drosophila* embryos was performed as described (Patel, 1994). Tissue fixation was done with 3.7 % formaldehyde in saline for 10 minutes at room temperature. Tissue was permeabilized through 3 sequential washes in PBT (0.075 M Phosphate Buffer, pH 7.2, 0,03% Triton x100), for 10 minutes each at RT. Primary and secondary staining was done overnight at 4°C, without preceeding blocking. The primary antibodies and dilutions are listed in the Key Resources Table. Secondary fluorophore-conjugated antibodies (Molecular Probes) were used at 1:600.

**Confocal Image Acquisition**

Flat-prepped immunostained embryos were mounted in Vectashield anti-fading medium (Vector Laboratories, USA). Image acquisition was performed on a Zeiss LSM 700 inverted confocal microscope, using a 40 X oil objective lens (1.3 NA). Z-stacks spanning the whole VNC thickness were acquired with a step size of 1 µm.

For live imaging, dechorionated stage 14 embryos were glued lateral or ventral side down on a MatTek glass bottom dish and they were covered with S100 Halocarbon Oil (Merck) to avoid desiccation. Image acquisition was performed on a Zeiss LSM 700 inverted confocal microscope, using a 25 X oil immersion lens (0.8 NA) and on a NikonA1Rsi, using a 20 X air lens (0.75 NA). Z-stacks spanning the whole VNC thickness, with a 2 µm step size, were acquired every 5 or 10 minutes, for a total of 8-16 hours.

**Light-Sheet Imaging**

Multi-view light-sheet imaging was performed on a custom-built setup. The design and imaging capabilities are similar to systems previously described (Krzic et al., 2012). Embryos were mounted in low-melting agar (0.8% w/v) filled inside FEP tube (wall

thickness 0.3 mm, inner diameter 0.5 mm, refractive index 1.3) and imaged through FEP tube submerged in sample chamber filled with PBS buffer. The sample was illuminated with a light-sheet created by two long working objectives (Olympus 10 X, 0.3 NA) on the opposite side and two orthogonal fluorescence collection objectives (Nikon, water-immersion, 25 X, 1.1NA, WD 2mm). The fluorescence signal was collected and the image formed by a tube lens (Nikon, f-200 mm) on two sCMOS cameras (Hamamatsu, ORCA-Flash4.0 V2, pixel resolution 2048 X 2048, effective pixel size at object space 0.26 μm). 100 images were collected (z- resolution 1.8-2.6 μm) at 5 min time interval. Embryos were rotated 90º at each time point in order to reconstruct the full embryo morphology (see (Krzic et al., 2012) for reconstruction details).

**Image detwitching**

To perform detwitching, we first generated, with Matlab, isotropic three-dimensional reconstructions of the embryo at each time point using 3D linear interpolation of z-stacks images. On a single time-point, we manually identified the most anterior, posterior and ventral positions of the condensing CNS. We used the built-in Matlab 3D affine transformation function to map these points to the xy-plane of the transformed image. We then chose a reference time point at the middle of the condensation process (when the VNC was positioned ventrally) and used the *imregtform* Matlab function to align the other images. This process allowed us to suppress 3D rotations due to muscle twitching. To moderate the effect of local rapid muscle contractions, we blurred the movies in space and time (Gaussian filter, pixel size 2 in x, y and time). Sample code is available on Github: https://github.com/tes24/CNS-Paper

**Correlations Data analysis**

Confocal Images were scaled to be isotropic in all axes. Viewed along the AP axis, images were cropped to include only the VNC, and then the VNC was split into 50 bins, corresponding to 1.65 μm length each. Within each bin, a maximum intensity projection was performed along the included planes in the z-axis. The Matlab function *imregister* was then used to perform image registration. The optimizer for *imregister* was defined with multimodal metric, tolerance of $10^{-6}$ and 500 iterations. Before image registration, the center of mass of the two images was aligned so to maximize image overlap.

To create the image correlation traces, the regions of high correlation were manually identified and then plotted considering the mean correlation along ± 1 row in the correlation matrices. The diagonal values were ignored. Traces were offset along AP axis to ensure maximum overlap of peaks.

**Atomic Force Microscopy**

Staged embryos were placed on top of positively charged glass slides to immobilize them on a rigid substrate. The embryos were immersed in PBS solution and dissected to expose the CNS allowing AFM measurements. Force-indentation curves were obtained with a custom-built AFM mounted on an inverted optical microscope (TE2000; Nikon). A 20 μm diameter polystyrene bead was glued to the end of a tip-less cantilever (nominal spring constant k= 0.01 N/m, Novascan Technologies, Ames, IA), which had previously been calibrated by thermal tune oscillation (Jorba et al., 2017). The cantilever was displaced in 3-D with nanometric resolution by means of piezo-actuators coupled to strain gauge sensors (Physik Instrumente, Karlsruhe, Germany) to measure the vertical position of the cantilever (z). The deflection of the cantilever (d) was measured with a quadrant photodiode (S4349, Hamamatsu, Japan) using the optical lever method. Before each slice measurement, the slope of a deflection-displacement d–z curve obtained from a bare region of the coverslip was used to calibrate the relationship between the photodiode signal and cantilever deflection. A linear calibration curve with a sharp contact point was taken as indicative of a clean undamaged tip. Force (F) on the cantilever was computed as Hookean linear spring:

$$F = k(d - d_0) \qquad \text{Eq. (3)}$$

where k is the cantilever spring constant. Indentation depth δ was defined as:

$$\delta = (z - z_0) - (d - d_0) \qquad \text{Eq. (4)}$$

where $d_0$ as is the deflection offset and $z_0$ the cantilever displacement when the tip contacts the surface of the sample. F-z curves were analyzed with the Hertz contact model for a sphere indenting a semi-infinite half space:

$$F = \frac{4E}{3(1-\nu^2)} R^{1/2} \delta^{3/2} \qquad \text{Eq. (5)}$$

where R is the bead radius (10 µm), E is the Young's modulus and ν is the Poisson's ratio (assumed to be 0.5). Eq. (3) can be expressed in terms of z and d as:

$$d = d_0 + \frac{4E}{3k(1-\nu^2)} R^{1/2}[(z - z_0) - (d - d_0)]^{3/2} \quad \text{Eq. (6)}$$

**Laser Ablation**

Laser ablation experiments were performed on a Zeiss microscope stand equipped with a spinning disk module (CSU-X1; Yokogawa), an EMCCD camera (Andor) and a custom built laser ablation system using a 355 nm pulsed laser with energy per pulse in the 20 µJoule regime and a pulse repetition of 1000 Hz (Mayer et al., 2010).

Linear ablations were performed with a 50 µm line oriented perpendicular to the VNC AP axis at different positions (intercommissural or intracommissural) between the $1^{st}/4^{th}$ abdominal segments, at different embryonic stages. The laser was focused on equally spread points (shots) on the ROI, with a density of 2 shots/µm. For each shot, 25 laser pulses were delivered. The ablation was done in a single plane, cutting the axonal network, where the entire region of interest could be acquired. To capture the rapid recoil of the ablated front, single plane images were acquired with 50 ms exposure and with a 100 ms interval between frames. Initial recoil velocity of the ablated region was computed for the estimation of mechanical stress in the tissue. During laser microsurgery, after the early tensile recoil, we did not monitor the late compressive recovery.

**Modeling**

The experimental velocity field extracted from the PIV analysis was mapped onto the closest nodes of the FE model of the VNC (**Figure 3F** and **Figure S3C**), which uses an initial geometry that resembles the VNC before condensation. Mechanical equilibrium is imposed in order to find the deformation of the whole computational domain.

A simple Maxwell rheological model was used for computing the stress values. After the FE discretization with 15800 linear hexahedral elements (**Figure S3C**), Cauchy's equilibrium equation $\nabla \cdot \boldsymbol{\sigma} = \mathbf{0}$ yields a system of ordinary differential equations (ODEs) in terms of the nodal displacement vector u:

$$\boldsymbol{C}\frac{d\boldsymbol{u}}{dt} + \boldsymbol{K}\boldsymbol{u} = 0 \qquad \text{Eq. (7)}$$

where $\boldsymbol{C}$ is the matrix with viscous contributions and $\boldsymbol{K}$ is the stiffness matrix gathering the measured elastic properties of the material. We used a Young' modulus of E=75 Pa and a viscous coefficient η=500 Pa.s, which gives a similar characteristic time τ to the one measured through laser ablation (**Figure 3E**). The ODE system in Eq. (7) was integrated with an implicit second order accurate Crank-Nicholson scheme. The mapping of the velocities and the implementation of the FE model were done in a custom code in Matlab. Code is available on Github: https://github.com/tes24/CNS-Paper.

After imposition of the measured velocity field, we interpreted the resulting viscoelastic stresses of the model as the active stress field of the tissue, necessary for undergoing the condensation process. From these total stresses in the three-dimensional domain of the VNC, we extracted the compressive stress peaks along the AP axis, and fitted their evolution with a fourth inverse degree polynomial (see **Figure 3F** showing the fitted lines, and **Figure S3D** also showing the stress peaks on the kymograph). Stress peaks evolve spatially, with a magnitude that is maintained due to the VNC condensation and concomitant tissue relaxation.

Characteristic times τ in **Figure 3E** have been computed by fitting the gap $d(t)$ in the recoil with an exponential function $d(t) = Ae^{-t/\tau} + B$.

The stability analysis shown in **Figure 4** is computed from the characteristic equation of the system of delay differential equations in Eq. (1) and (2) (see (Dawi and Munoz, 2021) for further details). The sensitivity analyses were carried out by fixing all the model parameters to the reference values ($\gamma$, $k_1$, $k_2$, $\eta$, $\delta t$) = (0.2, 0.01, 1.9, 15, 20), and varying one by one along the different intervals shown. Instead, the double sensitivity phase space plots in **Figure S5E-H** were generated by changing two of the parameters simultaneously within the range limits of the examined space. Code is available on Github: https://github.com/tes24/CNS-Paper.

## QUANTIFICATION AND STATISTICAL ANALYSIS

### Image Processing

Basic confocal image processing and analyses were performed using Fiji (Schindelin et al., 2012). Vitelline membrane autofluorescence was removed from confocal 4D images employing an ImageJ / Fiji automated macro approach (Boix-Fabres et al., 2019).

**Neuronal cell bodies Semi-Automated Segmentation and Cell Density Estimation**

For estimating VNC cell density, at different condensation phases, we performed 3D semi-automated segmentation from stills of time-lapse recordings. Stage 14 embryos, pan-neuronally expressing the nuclear-RFP marker Red Stinger (Elav-Gal4> UAS-Red Stinger), were imaged live by confocal microscopy, as described earlier. Z-stacks spanning the whole VNC thickness, with a 2μm step size, were acquired every 5 minutes, for a total of 16 hours. Condensation phases were identified and z-stacks for representative single time-points of each condensation phase were selected. The z-stacks were processed by the 2D Stardist segmentation algorithm in Fiji. 2D Stardist segmentation was performed using the Versatile (fluorescent nuclei) model, in default mode, with optimized post-processing threshold settings. VNC neuronal nuclei segmentations were manually corrected by digitally dissecting overlapping nuclei, where required. A second round of 2D Stardist analysis was executed for defining the perimeter of each neuronal nucleus and the coordinates of their centroids, at each z-slice. In-house Excel scripts were employed to link by proximity the centroids of individual sections on the XY plane between adjacent z-slices. This allowed the volumetric reconstruction of individual nuclei and to define their positions in the VNC in 3D. Nuclei that could not be linked in-between adjacent z-slices were discarded.

To calculate the local density, for each centroid we calculated the number of neighbors using Matlab within a sphere of 7.5μm radius, around the chosen centroid. We excluded centroids near the surface to minimize boundary effects.

**AFM Fitting**

E, $z_0$ and $d_0$ were computed for each force–indentation curve by non-linear least-squares fitting using custom built code (Matlab). The fitting was performed for the approaching force curve up to a maximum indentation of ~4 μm. At each measurement point, E was characterized as the average of the values computed from five force curves consecutively

obtained with ramp amplitude of 20 μm and frequency of 0.3 Hz. For each embryo, the Young's modulus (E) was measured at, at least, 3 positions along the antero-posterior axis in the midline and in lateral regions (left and right separated 20 μm from the midline).

**Laser Ablation data analysis**

The images obtained from the laser ablations were analyzed using Fiji and Matlab. Kymographs were drawn on both sides (proximal- and distal) of the ablated line using the FIJI plugin Multi Kymograph (Schindelin et al., 2012). Both recoil velocities were calculated using a custom written routine in Matlab. The final recoil velocity ($V_{average}$) for one ablation was computed as the average of the recoil velocities that are both proximal-oriented ($V_{proximal}$) and distal-oriented ($V_{distal}$):

$$V_{avg} = (V_{proximal} + V_{distal}) / 2$$

We performed an exponential fitting of experimental recoil curves $y(t)$ to a function describing the relaxation of a viscoelastic tissue

$$y(t)=y_0 + (y_\infty - y_0)\,(1-\exp(-t/\tau)) \qquad \text{Eq. (8)}$$

where $y_0$ is the initial opening, $y_\infty$ measures the recoil increment (or tissue contractility) and $\tau$ is the characteristic time which is proportional to tissue viscosity.

**Particle Image Velocimetry (PIV) and Strain rates calculation**

Tissue displacements were analyzed by tracer particles, which in our experiments were EGFP-labeled Fas2 molecules and mCherry-labeled Histone2Av molecules. Flow fields were quantitatively measured using the open-source tool for Matlab PIVlab (Thielicke and Stamhuis, 2018). The software calculated the displacement of the tracers between pairs of images (sequential time points) using the Fast Fourier Transformation algorithm with multiple passes and deforming windows. We also wrote custom software for performing the PIV analysis on the light-sheet microscopy data, which is available on Github: https://github.com/tes24/CNS-Paper.

From the PIV results, the strain rate is then calculated by taking the spatial derivative of the PIV field after Gaussian smoothing (in both space and time) to reduce effects of noise. Code is available on Github: https://github.com/tes24/CNS-Paper.

## Statistical Tests

Statistical tests were performed using Matlab and estimationstats.com. Kolmogorov-Smirnov test was performed to test whether the observed values where normally distributed. When the distribution was normal, Student's t-test was performed to estimate significance of the quantities. In case the values are not normally distributed, non-parametric Mann-Whitney U-test was performed to estimate the significance of differences between the quantities. The corresponding p-values and the method used to estimate them are mentioned in the Figure legends.

## KEY RESOURCES TABLE

| REAGENT or RESOURCE | SOURCE | IDENTIFIER |
|---|---|---|
| **Antibodies** | | |
| Mouse monoclonal anti-acetylated Tubulin (1:2000) | Sigma Aldrich | T7451 |
| Rabbit anti-Non Muscle Myosin II (1:500) | D. Kiehart | (Kiehart and Feghali, 1986) |
| Mouse anti-Fas2 (1:100) | DHSB | clone 1D4 |
| Rabbit anti-Dcp-1 (Asp216) (1:100) | Cell Signaling | #9578 |
| Rabbit anti-GFP tag polyclonal (1:600) | Thermo Fisher Scientific | A-11122 |
| Rat anti-Elav (1:1000), DHSB | DHSB | clone 7E8A10 |
| Mouse anti-Repo (1:100) | DHSB | clone 8D12 |
| Goat anti-Rabbit IgG (H+L) Alexa Fluor 488 conjugate ((1:600) | Invitrogen | A-11008 |
| Goat anti-Rabbit IgG (H+L) Alexa Fluor 555 conjugate ((1:600) | Invitrogen | A-21428 |
| Goat anti-Mouse IgG (H+L) Alexa Fluor 488 conjugate ((1:600) | Invitrogen | A-11001 |

| | | |
|---|---|---|
| Goat anti-Mouse IgG (H+L) Alexa Fluor 555 conjugate ((1:600) | Invitrogen | A-21422 |
| Goat anti-Rat IgG (H+L) Alexa Fluor 488 conjugate ((1:600) | Invitrogen | A11006 |
| Phalloidin-TRITC staining (1:1000)). | Sigma Aldrich | P1951 |
| **Experimental models: *Drosophila* strains** | | |
| *w1118, fas2-GFP$^{CB03616}$* | Dr. Christian Klämbt | |
| *w, elav-Gal4 [C155]* | BDSC | #6923 |
| *w; ; repo-Gal4 / TM3, Sb[1]* | BDSC | #7415 |
| *w; ; pino1::Repo-Gal4::UAS-mCD8-GFP / TM6B, Dfd-GMR-nv-YFP, Sb[1], Tb[1]* | Dr. Gerald Udolph | |
| *w; ; pino1::Repo-Gal4::UAS-mCD8-GFP:: His2Av-mRFP / TM6B, Dfd-GMR-nv-YFP, Sb[1], Tb[1]* | This work | |
| *w; ; pino1::elav-mCD8-GFP / TM6B, Dfd-GMR-nv-YFP, Sb[1], Tb[1]* | Dr. Gerald Udolph | |
| *w; moody-Gal4:UAS-mCD8-GFP* | Dr. Christian Klämbt | |
| *w; UAS-zipper RNAi / CyO* | BDSC | #37480 |
| *w; His2Av-mRFP* | BDSC | #23651 |
| *w; His2Av-mCherry* | Dr. Lars Hufnagel | |
| *w, alpha-tubulin-GFP; H2Av-mRFP* | Dr. Elena Rebollo | |
| *w; if / CyO; UAS-GRIM* | Dr. Todd Laverty | |
| *w; {UAS-Red Stinger}4/CyO* | BDSC | #8546 |
| *w* | BDSC | #3605 |
| **Software and algorithms** | | |
| Fiji | (Schindelin et al., 2012) | https://imagej.net/software/fiji/ |
| Matlab | MATLAB ® | |
| Rheological Model (Stability analysis Delay Code) | (Dawi and Munoz, 2021) | |
| FEM (stress/strain analysis) Code | This paper | https://github.com/tes24/CNS-Paper |
| Rheological Model (Sensitivity analysis Code) | This paper | https://github.com/tes24/CNS-Paper |

| | | |
|---|---|---|
| Detwitching Code | This paper | https://github.com/tes24/CNS-Paper |
| Custom PIV Code | This paper | https://github.com/tes24/CNS-Paper |
| Custom Strain Code | This paper | https://github.com/tes24/CNS-Paper |

## SUPPLEMENTARY MOVIES LEGENDS

**Movie S1. VNC Cytoskeleton structural organization, Related to Figures 6 and S1**

Animated 3D reconstruction of a section of the VNC of a late *Drosophila* embryo (Stage 16) highlighting the levels of expression (Fire Lut) of different cytoskeletal components: the axonal pattern stained with anti Acetylated α-Tubulin antibodies (left); the iterated segmental distribution of actin (Phalloidin staining) along the AP axis (centre); and the distribution of NMM accumulating at the longitudinal dorsomedial edges of the neuropile. Scale bar 15 μm.

**Movie S2. Dynamics of VNC condensation, Related to Figures 1, 2 and S2**

From top to bottom:

- Time lapse of an elav-Gal4>UASmCD8-GFP embryo (lateral view) recorded by confocal microscopy. mCD8-GFP labeling marks all neural derivatives. AP axis orientation is indicated. Time in hours. Scale bar 50 μm.
- Time lapse recorded by multi-view light-sheet imaging of a live Histone2Av-mCherry embryo (ventral view). mCherry labeling marks all nuclei and was used to correct the embryo twitching. Raw data is shown on the top and "detwitched" images on the bottom. AP axis orientation is indicated. Time in hours. Scale bar 50μm.
- Time Lapse recording of an embryo expressing Fas2-GFP (Top - ventral view; Bottom - re-slice over the Z-axis) acquired by Confocal Microscopy. The double headed arrow points to the stationary domain where converge anterior and posterior condensation. AP axis orientation is indicated. Time in hours. Scale bar 50μm.

**Movie S3. VNC response to laser microsurgery during condensation, Related to Figures 3 and S4**

From top to bottom:

- Laser ablation of stage 14 embryos expressing alpha Tubulin-GFP. The recoil of intercommissural (left) and intracommissural (right) cuts are compared. Yellow lines highlight the position of the laser cuts. AP axis orientation is indicated. Time in seconds. Scale bar 20μm.
- Evolution over time of a laser cut at the intercommissural space between the abdominal segments A1 and A2, of a stage 14 embryo, expressing alpha Tubulin-GFP. After ablation, the individual neuromeres (color coded dots at the bottom mark the positions of the anterior and posterior commissures of each neuromere at sequential times) continue to condense autonomously. Yellow line highlights the position of the laser cut. AP axis orientation is indicated. Time in hours. Scale bar 20μm.

**Movie S4. Three-dimensional Finite Element model (FE), Related to Figures 3 and S4**

The measured velocity field was mapped onto the FE model to reconstruct strain and stress fields. Evolution through time of contour plots of AP stresses $\sigma''''$ (FE model) superimposed over experimental live images (ventral view) of an embryo expressing Fas2-GFP. AP axis orientation is indicated. Time in hours. Scale bar 50μm.

**Movie S5. Glia participates in the architectural organization of the VNC and its condensation, Related to Figures 5 and S6**

From top to bottom:

- Time lapse recordings of WT (Top) and Repo-Gal4>UAS-Grim (bottom) embryos in an alpha Tubulin-GFP background (ventral view) acquired by Confocal Microscopy. AP axis orientation is indicated. Time in hours. Scale bar 50μm.
- Light-sheet imaging record of a Repo-Gal4::UAS-mCD8-GFP::His2Av-mRFP>UAS-Grim embryo (ventral view) at different times of development (Stages

15-17). Magenta arrows denote local velocity trajectories from PIV analyses. The VNC is significantly elongated and misshaped. AP axis orientation is indicated. Time in hours. Scale bar 50 μm.

**Movie S6. Distinct roles for neurons and glia in VNC architecture and condensation, Related to Figure 6**

Time lapse recordings of embryos expressing Fas2-GFP, monitored by confocal imaging. From top to bottom, condensation dynamics in control (WT); Elav-Gal4>UAS-Zip-RNAi and Repo-Gal4>UAS-Zip-RNAi embryos. AP axis orientation is indicated. Time in hours. Scale bar 50 μm.

**Movie S7. Finite Element model of VNC condensation: Myosin-mediated contractility, Related to Figures 6 and 7**

From top to bottom:

- Three-dimensional representation of VNC condensation. FE model showing the evolution through time of contour plots of AP displacements (top) and experimental live images (ventral view) of an embryo expressing Fas2-GFP (bottom). AP axis orientation is indicated. Time in hours.
- Finite element simulations with mapped velocities of control (WT); Elav-Gal4>UAS-Zip-RNAi and Repo-Gal4>UAS-Zip-RNAi embryos. Contour plots in the top row show the AP displacement fields and in the bottom row the elastic strains ε_xx.

**REFERENCES**

Amourda, C., and Saunders, T.E. (2017). Gene expression boundary scaling and organ size regulation in the Drosophila embryo. Dev Growth Differ *59*, 21-32.

Anava, S., Greenbaum, A., Ben Jacob, E., Hanein, Y., and Ayali, A. (2009). The regulative role of neurite mechanical tension in network development. Biophys J *96*, 1661-1670.

1070 Barriga, E.H., Franze, K., Charras, G., and Mayor, R. (2018). Tissue stiffening
1071 coordinates morphogenesis by triggering collective cell migration in vivo. Nature *554*,
1072 523-527.

1073 Beckervordersandforth, R.M., Rickert, C., Altenhein, B., and Technau, G.M. (2008).
1074 Subtypes of glial cells in the Drosophila embryonic ventral nerve cord as related to
1075 lineage and gene expression. Mech Dev *125*, 542-557.

1076 Bertet, C., Sulak, L., and Lecuit, T. (2004). Myosin-dependent junction remodelling
1077 controls planar cell intercalation and axis elongation. Nature *429*, 667-671.

1078 Boix-Fabres, J., Karkali, K., Martin-Blanco, E., and Rebollo, E. (2019). Automated
1079 Macro Approach to Remove Vitelline Membrane Autofluorescence in Drosophila
1080 Embryo 4D Movies. Methods Mol Biol *2040*, 155-175.

1081 Bullmore, E., and Sporns, O. (2012). The economy of brain network organization. Nat
1082 Rev Neurosci *13*, 336-349.

1083 Bullock, T.H., and Horridge, G.A. (1965). Structure and function in the nervous systems
1084 of invertebrates (San Francisco: W. H. Freeman).

1085 Buszczak, M., Paterno, S., Lighthouse, D., Bachman, J., Planck, J., Owen, S., Skora,
1086 A.D., Nystul, T.G., Ohlstein, B., Allen, A.*, et al.* (2007). The carnegie protein trap library:
1087 a versatile tool for Drosophila developmental studies. Genetics *175*, 1505-1531.

1088 Cajal, S.R.y. (1899). Textura del Sistema Nervioso del Hombre y de los Vertebrados
1089 (Madrid, Spain: Nicolas Moya).

1090 Campos-Ortega, J.A., and Hartenstein, V. (1985). The embryonic development of
1091 Drosophila melanogaster (Berlin ; New York: Springer-Verlag).

1092 Cavanaugh, K.E., Staddon, M.F., Munro, E., Banerjee, S., and Gardel, M.L. (2020).
1093 RhoA Mediates Epithelial Cell Shape Changes via Mechanosensitive Endocytosis. Dev
1094 Cell *52*, 152-166 e155.

1095 Chen, P., Nordstrom, W., Gish, B., and Abrams, J.M. (1996). grim, a novel cell death
1096 gene in Drosophila. Genes Dev *10*, 1773-1782.

1097 Christley, S., Alber, M.S., and Newman, S.A. (2007). Patterns of mesenchymal
1098 condensation in a multiscale, discrete stochastic model. PLoS Comput Biol *3*, e76.

1099 Clement, R., Dehapiot, B., Collinet, C., Lecuit, T., and Lenne, P.F. (2017). Viscoelastic
1100 Dissipation Stabilizes Cell Shape Changes during Tissue Morphogenesis. Curr Biol *27*,
1101 3132-3142 e3134.

Dawi, M.A., and Munoz, J.J. (2021). Stability bounds of a delay visco-elastic rheological model with substrate friction. J Math Biol *83*, 71.

DeLise, A.M., Fischer, L., and Tuan, R.S. (2000). Cellular interactions and signaling in cartilage development. Osteoarthr Cartil *8*, 309-334.

Doubrovinski, K., Swan, M., Polyakov, O., and Wieschaus, E.F. (2017). Measurement of cortical elasticity in Drosophila melanogaster embryos using ferrofluids. Proc Natl Acad Sci U S A *114*, 1051-1056.

Erneux, T. (2009). Applied delay differential equations (New York: Springer).

Evans, I.R., Hu, N., Skaer, H., and Wood, W. (2010). Interdependence of macrophage migration and ventral nerve cord development in Drosophila embryos. Development *137*, 1625-1633.

Franze, K. (2013). The mechanical control of nervous system development. Development *140*, 3069-3077.

Franze, K., Janmey, P.A., and Guck, J. (2013). Mechanics in neuronal development and repair. Annu Rev Biomed Eng *15*, 227-251.

Frenz, D.A., Jaikaria, N.S., and Newman, S.A. (1989). The mechanism of precartilage mesenchymal condensation: a major role for interaction of the cell surface with the amino-terminal heparin-binding domain of fibronectin. Dev Biol *136*, 97-103.

Hall, B.K., and Miyake, T. (2000). All for one and one for all: condensations and the initiation of skeletal development. Bioessays *22*, 138-147.

Hartenstein, V., and Wodarz, A. (2013). Initial neurogenesis in Drosophila. Wiley Interdiscip Rev Dev Biol *2*, 701-721.

Heisenberg, C.-P., and Bellaïche, Y. (2013). Forces in Tissue Morphogenesis and Patterning. Cell *153*, 948-962.

Hogan, B.L. (1999). Morphogenesis. Cell *96*, 225-233.

Ito, K., Urban, J., and Technau, G.M. (1995). Distribution, classification, and development ofDrosophila glial cells in the late embryonic and early larval ventral nerve cord. Rouxs Arch Dev Biol *204*, 284-307.

Jorba, I., Uriarte, J.J., Campillo, N., Farre, R., and Navajas, D. (2017). Probing Micromechanical Properties of the Extracellular Matrix of Soft Tissues by Atomic Force Microscopy. J Cell Physiol *232*, 19-26.

Karkali, K., Saunders, T.E., Vernon, S.W., Baines, R.A., Panayotou, G., and Martín-Blanco, E. (2020). JNK signaling in pioneer neurons directs the architectural organization of the CNS and coordinates the motor activity of the Drosophila embryo. bioRxiv, 092486.

Khalilgharibi, N., Fouchard, J., Asadipour, N., Barrientos, R., Duda, M., Bonfanti, A., Yonis, A., Harris, A., Mosaffa, P., and Fujita, Y. (2019). Stress relaxation in epithelial monolayers is controlled by the actomyosin cortex. Nat Physics *15*, 839-847.

Kiehart, D.P., and Feghali, R. (1986). Cytoplasmic myosin from Drosophila melanogaster. J Cell Biol *103*, 1517-1525.

Kilinc, D. (2018). The Emerging Role of Mechanics in Synapse Formation and Plasticity. Front Cell Neurosci *12*, 483.

Krzic, U., Gunther, S., Saunders, T.E., Streichan, S.J., and Hufnagel, L. (2012). Multiview light-sheet microscope for rapid in toto imaging. Nat Methods *9*, 730-733.

Landgraf, M., Bossing, T., Technau, G.M., and Bate, M. (1997). The origin, location, and projections of the embryonic abdominal motorneurons of Drosophila. J Neurosci *17*, 9642-9655.

Landgraf, M., Sanchez-Soriano, N., Technau, G.M., Urban, J., and Prokop, A. (2003). Charting the Drosophila neuropile: a strategy for the standardised characterisation of genetically amenable neurites. Dev Biol *260*, 207-225.

Le Novère, N. (2015). Quantitative and logic modelling of molecular and gene networks. Nature Reviews Genetics *16*, 146-158.

LeGoff, L., and Lecuit, T. (2015). Mechanical Forces and Growth in Animal Tissues. Cold Spring Harb Perspect Biol *8*, a019232.

Li, Y., Muffat, J., Omer, A., Bosch, I., Lancaster, M.A., Sur, M., Gehrke, L., Knoblich, J.A., and Jaenisch, R. (2017). Induction of Expansion and Folding in Human Cerebral Organoids. Cell Stem Cell *20*, 385-396 e383.

Lin, D.M., Fetter, R.D., Kopczynski, C., Grenningloh, G., and Goodman, C.S. (1994). Genetic analysis of Fasciclin II in Drosophila: defasciculation, refasciculation, and altered fasciculation. Neuron *13*, 1055-1069.

Lynch, H.E., Crews, S.M., Rosenthal, B., Kim, E., Gish, R., Echiverri, K., and Hutson, M.S. (2013). Cellular mechanics of germ band retraction in Drosophila. Dev Biol *384*, 205-213.

1165 Mammoto, T., and Ingber, D.E. (2010). Mechanical control of tissue and organ
1166 development. Development *137*, 1407-1420.

1167 Martinek, N., Shahab, J., Saathoff, M., and Ringuette, M. (2008). Haemocyte-derived
1168 SPARC is required for collagen-IV-dependent stability of basal laminae in Drosophila
1169 embryos. J Cell Sci *121*, 1671-1680.

1170 Matsubayashi, Y., Sanchez-Sanchez, B.J., Marcotti, S., Serna-Morales, E., Dragu, A.,
1171 Diaz-de-la-Loza, M.D., Vizcay-Barrena, G., Fleck, R.A., and Stramer, B.M. (2020).
1172 Rapid Homeostatic Turnover of Embryonic ECM during Tissue Morphogenesis. Dev
1173 Cell *54*, 33-42 e39.

1174 Mayer, M., Depken, M., Bois, J.S., Julicher, F., and Grill, S.W. (2010). Anisotropies in
1175 cortical tension reveal the physical basis of polarizing cortical flows. Nature *467*, 617-
1176 621.

1177 Meyer, S., Schmidt, I., and Klambt, C. (2014). Glia ECM interactions are required to
1178 shape the Drosophila nervous system. Mech Dev *133*, 105-116.

1179 Miller, C.J., and Davidson, L.A. (2013). The interplay between cell signalling and
1180 mechanics in developmental processes. Nat Rev Genet *14*, 733-744.

1181 Mongera, A., Rowghanian, P., Gustafson, H.J., Shelton, E., Kealhofer, D.A., Carn, E.K.,
1182 Serwane, F., Lucio, A.A., Giammona, J., and Campas, O. (2018). A fluid-to-solid
1183 jamming transition underlies vertebrate body axis elongation. Nature *561*, 401-405.

1184 Muñoz, J.J., Dingle, M., and Wenzel, M. (2018). Mechanical oscillations in biological
1185 tissues as a result of delayed rest-length changes. Phys Rev E *98*, 052409.

1186 Negrete, J., and Oates, A.C. (2021). Towards a physical understanding of developmental
1187 patterning. Nature Reviews Genetics *22*, 518-531.

1188 Notbohm, J., Banerjee, S., Utuje, K.J.C., Gweon, B., Jang, H., Park, Y., Shin, J., Butler,
1189 J.P., Fredberg, J.J., and Marchetti, M.C. (2016). Cellular Contraction and Polarization
1190 Drive Collective Cellular Motion. Biophys J *110*, 2729-2738.

1191 Novák, B., and Tyson, J.J. (2008). Design principles of biochemical oscillators. Nature
1192 Reviews Molecular Cell Biology *9*, 981-991.

1193 Oliveira, M.M., Shingleton, A.W., and Mirth, C.K. (2014). Coordination of wing and
1194 whole-body development at developmental milestones ensures robustness against
1195 environmental and physiological perturbations. PLoS Genet *10*, e1004408.

1196 Olofsson, B., and Page, D.T. (2005). Condensation of the central nervous system in
1197 embryonic Drosophila is inhibited by blocking hemocyte migration or neural activity.
1198 Dev Biol *279*, 233-243.

1199 Page, D.T., and Olofsson, B. (2008). Multiple roles for apoptosis facilitating
1200 condensation of the Drosophila ventral nerve cord. Genesis *46*, 61-68.

1201 Pastor-Pareja, J.C., and Xu, T. (2011). Shaping cells and organs in Drosophila by
1202 opposing roles of fat body-secreted Collagen IV and perlecan. Dev Cell *21*, 245-256.

1203 Patel, N.H. (1994). Imaging neuronal subsets and other cell types in whole-mount
1204 Drosophila embryos and larvae using antibody probes. Methods Cell Biol *44*, 445-487.

1205 Petridou, N.I., and Heisenberg, C.P. (2019). Tissue rheology in embryonic organization.
1206 EMBO J *38*, e102497.

1207 Petrolli, V., Le Goff, M., Tadrous, M., Martens, K., Allier, C., Mandula, O., Herve, L.,
1208 Henkes, S., Sknepnek, R., Boudou, T.*, et al.* (2019). Confinement-Induced Transition
1209 between Wavelike Collective Cell Migration Modes. Phys Rev Lett *122*, 168101.

1210 Peyret, G., Mueller, R., d'Alessandro, J., Begnaud, S., Marcq, P., Mege, R.M., Yeomans,
1211 J.M., Doostmohammadi, A., and Ladoux, B. (2019). Sustained Oscillations of Epithelial
1212 Cell Sheets. Biophys J *117*, 464-478.

1213 Pipa, R.L. (1973). Proliferation, movement, and regression of neurons during the
1214 postembryonic development of insects. In Developmental Neurobiology of Arthropods
1215 (Cambridge: Cambridge University Press).

1216 Redies, C., and Puelles, L. (2001). Modularity in vertebrate brain development and
1217 evolution. Bioessays *23*, 1100-1111.

1218 Roig-Puiggros, S., Vigouroux, R.J., Beckman, D., Bocai, N.I., Chiou, B., Davimes, J.,
1219 Gomez, G., Grassi, S., Hoque, A., Karikari, T.K.*, et al.* (2020). Construction and
1220 reconstruction of brain circuits: normal and pathological axon guidance. J Neurochem
1221 *153*, 10-32.

1222 Sanchez-Soriano, N., Tear, G., Whitington, P., and Prokop, A. (2007). Drosophila as a
1223 genetic and cellular model for studies on axonal growth. Neural Dev *2*, 9.

1224 Saunders, T.E., and Ingham, P.W. (2019). Open questions: how to get developmental
1225 biology into shape? BMC Biol *17*, 17.

Schindelin, J., Arganda-Carreras, I., Frise, E., Kaynig, V., Longair, M., Pietzsch, T., Preibisch, S., Rueden, C., Saalfeld, S., Schmid, B.*, et al.* (2012). Fiji: an open-source platform for biological-image analysis. Nat Methods *9*, 676-682.

Schwabe, T., Li, X., and Gaul, U. (2017). Dynamic analysis of the mesenchymal-epithelial transition of blood-brain barrier forming glia in Drosophila. Biol Open *6*, 232-243.

Serwane, F., Mongera, A., Rowghanian, P., Kealhofer, D.A., Lucio, A.A., Hockenbery, Z.M., and Campas, O. (2017). In vivo quantification of spatially varying mechanical properties in developing tissues. Nat Methods *14*, 181-186.

Shellard, A., and Mayor, R. (2021). Collective durotaxis along a self-generated stiffness gradient in vivo. Nature *600*, 690-694.

Shyer, A.E., Rodrigues, A.R., Schroeder, G.G., Kassianidou, E., Kumar, S., and Harland, R.M. (2017). Emergent cellular self-organization and mechanosensation initiate follicle pattern in the avian skin. Science *357*, 811-815.

Singh, P., and Schwarzbauer, J.E. (2012). Fibronectin and stem cell differentiation - lessons from chondrogenesis. J Cell Sci *125*, 3703-3712.

Solon, J., Kaya-Copur, A., Colombelli, J., and Brunner, D. (2009). Pulsed forces timed by a ratchet-like mechanism drive directed tissue movement during dorsal closure. Cell *137*, 1331-1342.

Spedden, E., and Staii, C. (2013). Neuron biomechanics probed by atomic force microscopy. Int J Mol Sci *14*, 16124-16140.

Staddon, M.F., Cavanaugh, K.E., Munro, E.M., Gardel, M.L., and Banerjee, S. (2019). Mechanosensitive Junction Remodeling Promotes Robust Epithelial Morphogenesis. Biophys J *117*, 1739-1750.

Stark, M.R., Sechrist, J., Bronner-Fraser, M., and Marcelle, C. (1997). Neural tube-ectoderm interactions are required for trigeminal placode formation. Development *124*, 4287-4295.

Stépán, G. (1989). Retarded dynamical systems : stability and characteristic functions (Harlow: Longman Scientific and Technical).

Sumi, A., Hayes, P., D'Angelo, A., Colombelli, J., Salbreux, G., Dierkes, K., and Solon, J. (2018). Adherens Junction Length during Tissue Contraction Is Controlled by the

Mechanosensitive Activity of Actomyosin and Junctional Recycling. Dev Cell *47*, 453-463 e453.

Swanson, L.W. (2007). Quest for the basic plan of nervous system circuitry. Brain Res Rev *55*, 356-372.

Technau, G.M. (2008). Brain development in Drosophila melanogaster, Vol 628 (Springer Science+Business Media, LLC - Landes Bioscience).

Tessier-Lavigne, M., and Goodman, C.S. (1996). The molecular biology of axon guidance. Science *274*, 1123-1133.

Thielicke, W., and Stamhuis, E.J. (2018). The effects of wing twist in slow-speed flapping flight of birds: trading brute force against efficiency. Bioinspir Biomim *13*, 056015.

Tiwari, P., Rengarajan, H., and Saunders, T.E. (2021). Scaling of internal organs during Drosophila embryonic development. Biophys J *120*, 4264-4276.

Vig, D.K., Hamby, A.E., and Wolgemuth, C.W. (2016). On the Quantification of Cellular Velocity Fields. Biophys J *110*, 1469-1475.

Weber, G.F., Bjerke, M.A., and DeSimone, D.W. (2011). Integrins and cadherins join forces to form adhesive networks. J Cell Sci *124*, 1183-1193.

Zhang, H., and Labouesse, M. (2012). Signalling through mechanical inputs: a coordinated process. J Cell Sci *125*, 3039-3049.

Zlatic, M., Li, F., Strigini, M., Grueber, W., and Bate, M. (2009). Positional cues in the Drosophila nerve cord: semaphorins pattern the dorso-ventral axis. PLoS Biol *7*, e1000135.

# Figure 1

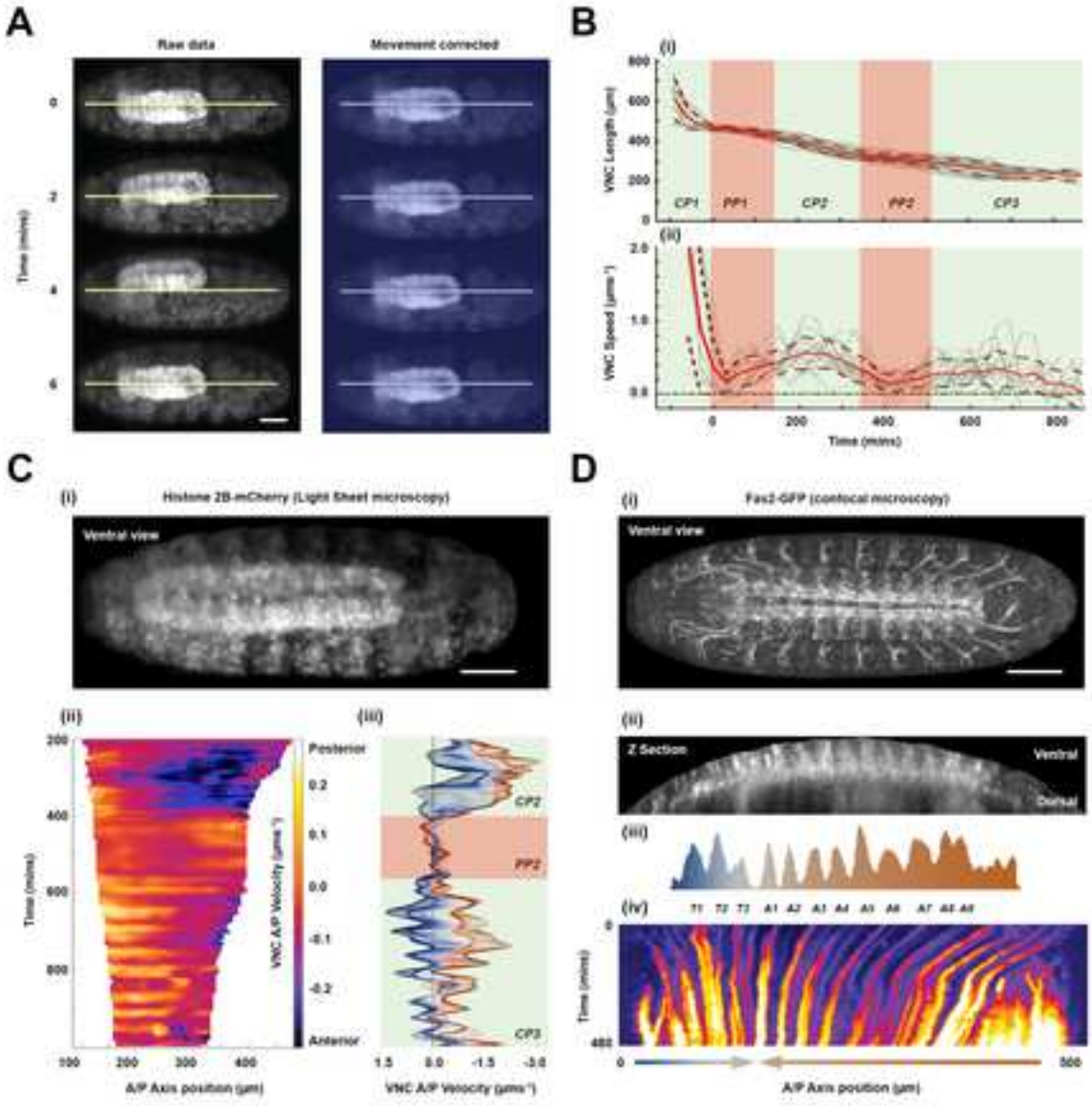

# Figure 2

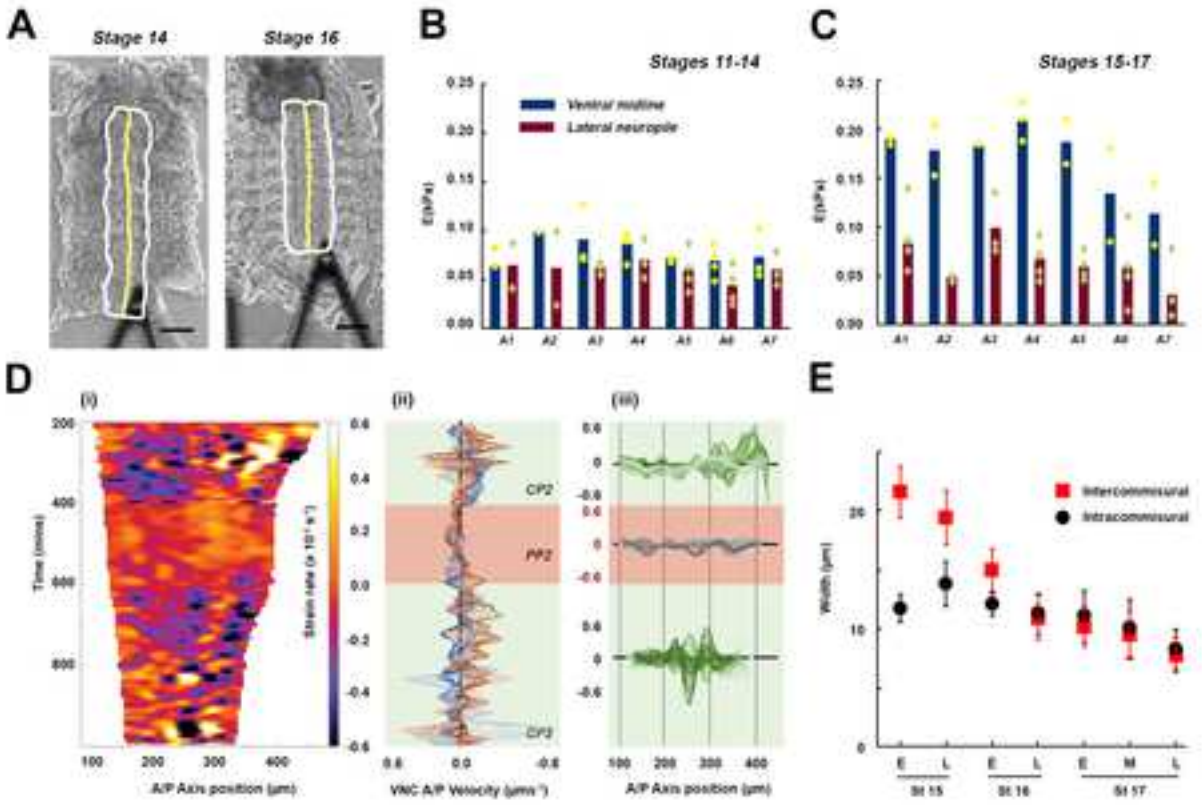

# Figure 3

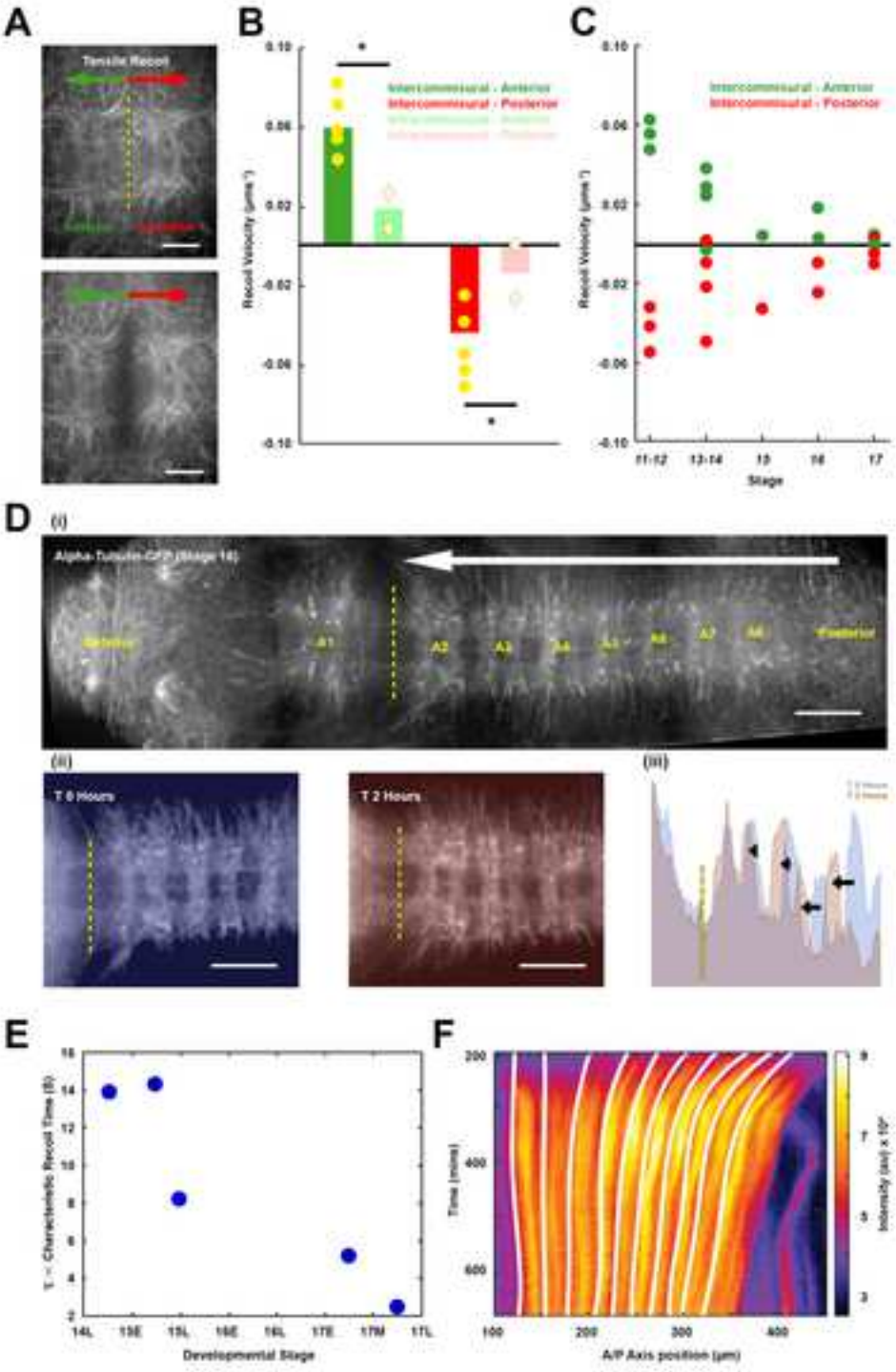

# Figure 4

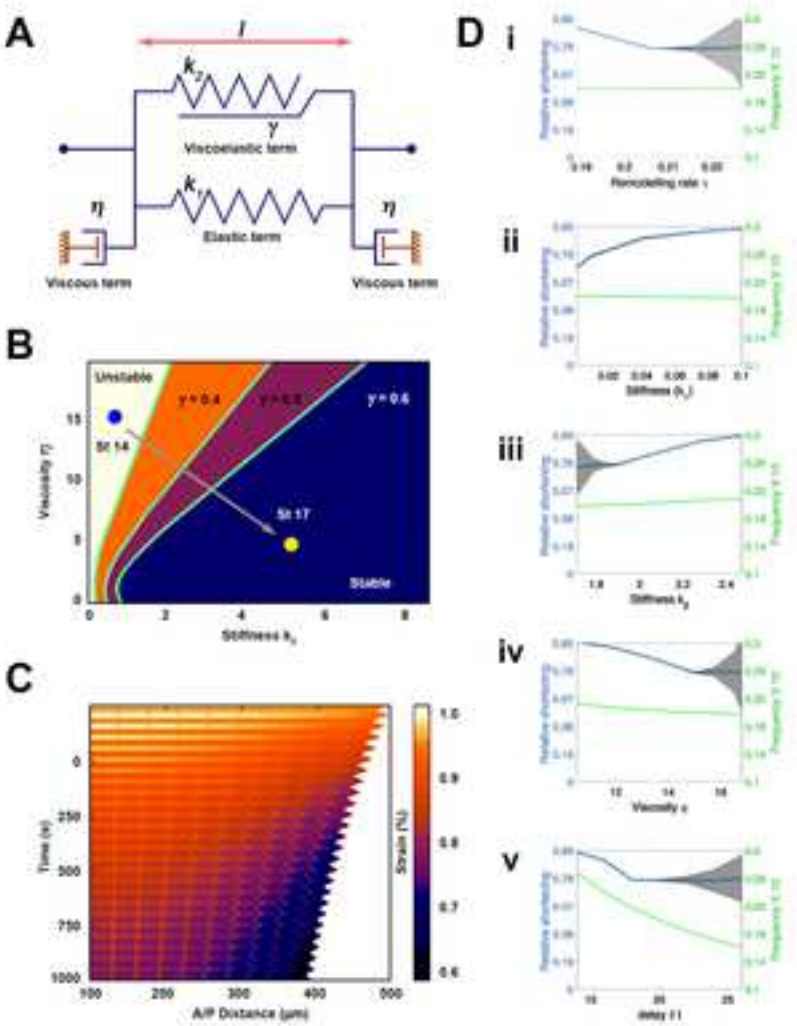

# Figure 5

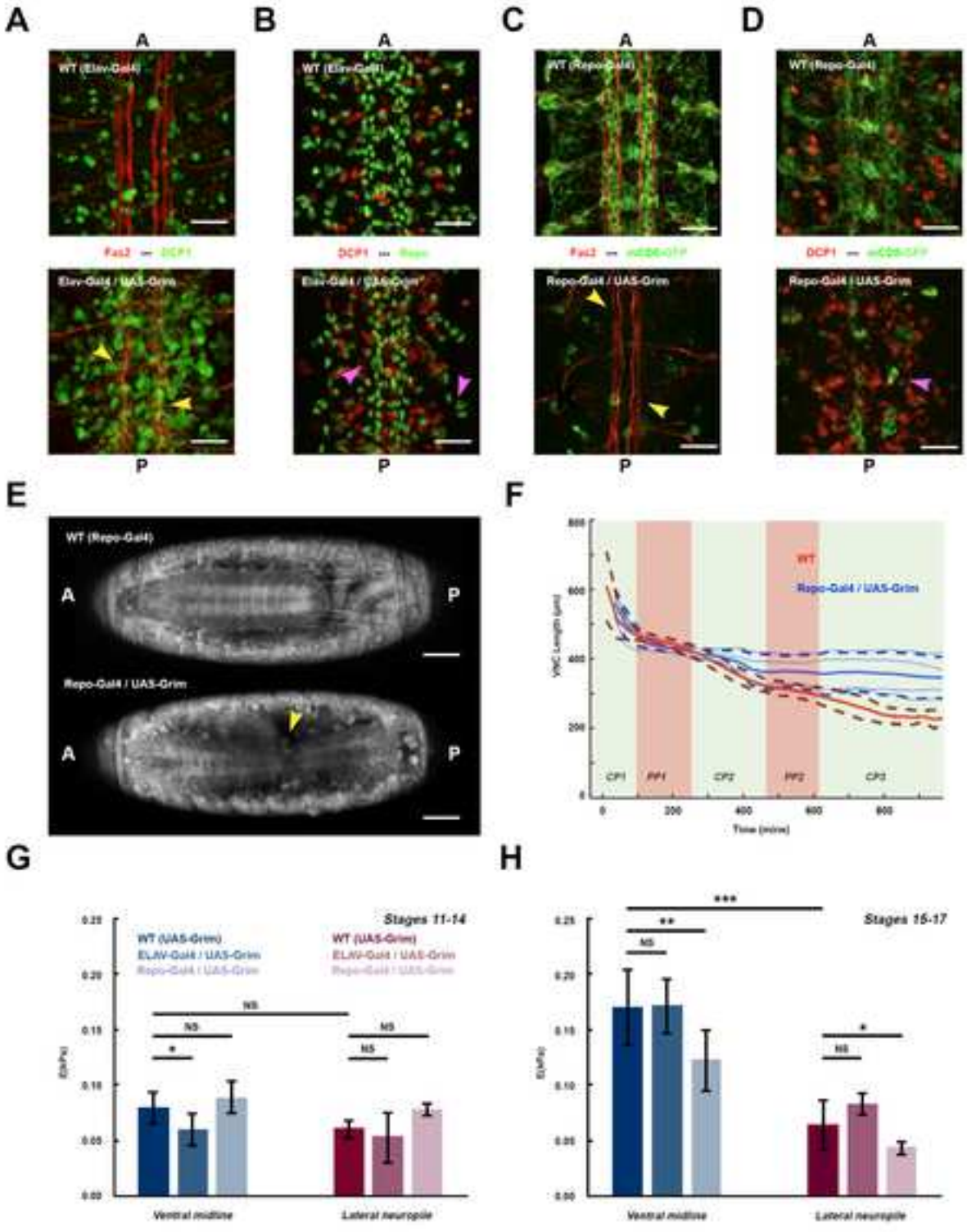

# Figure 6

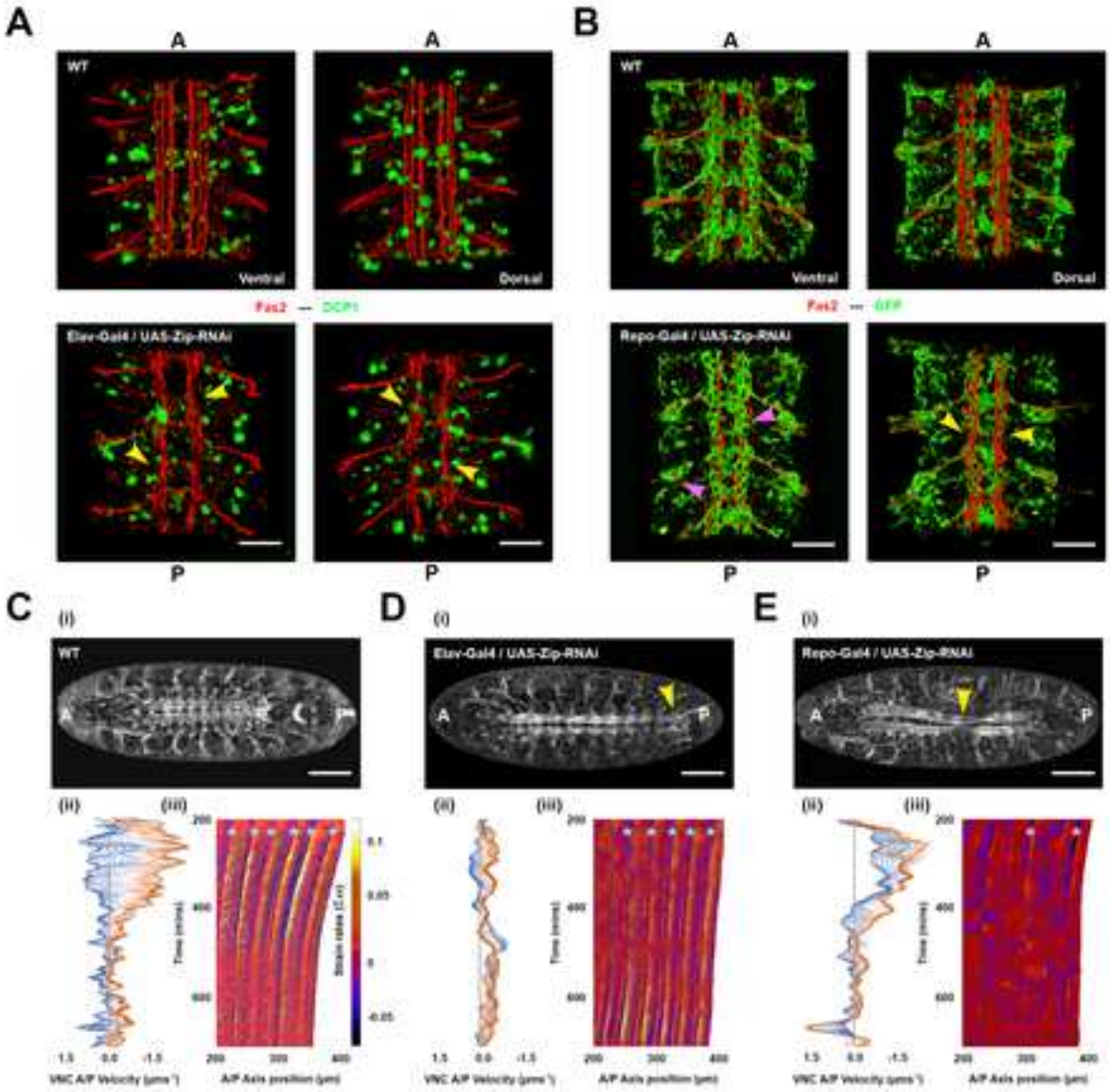

# Figure 7

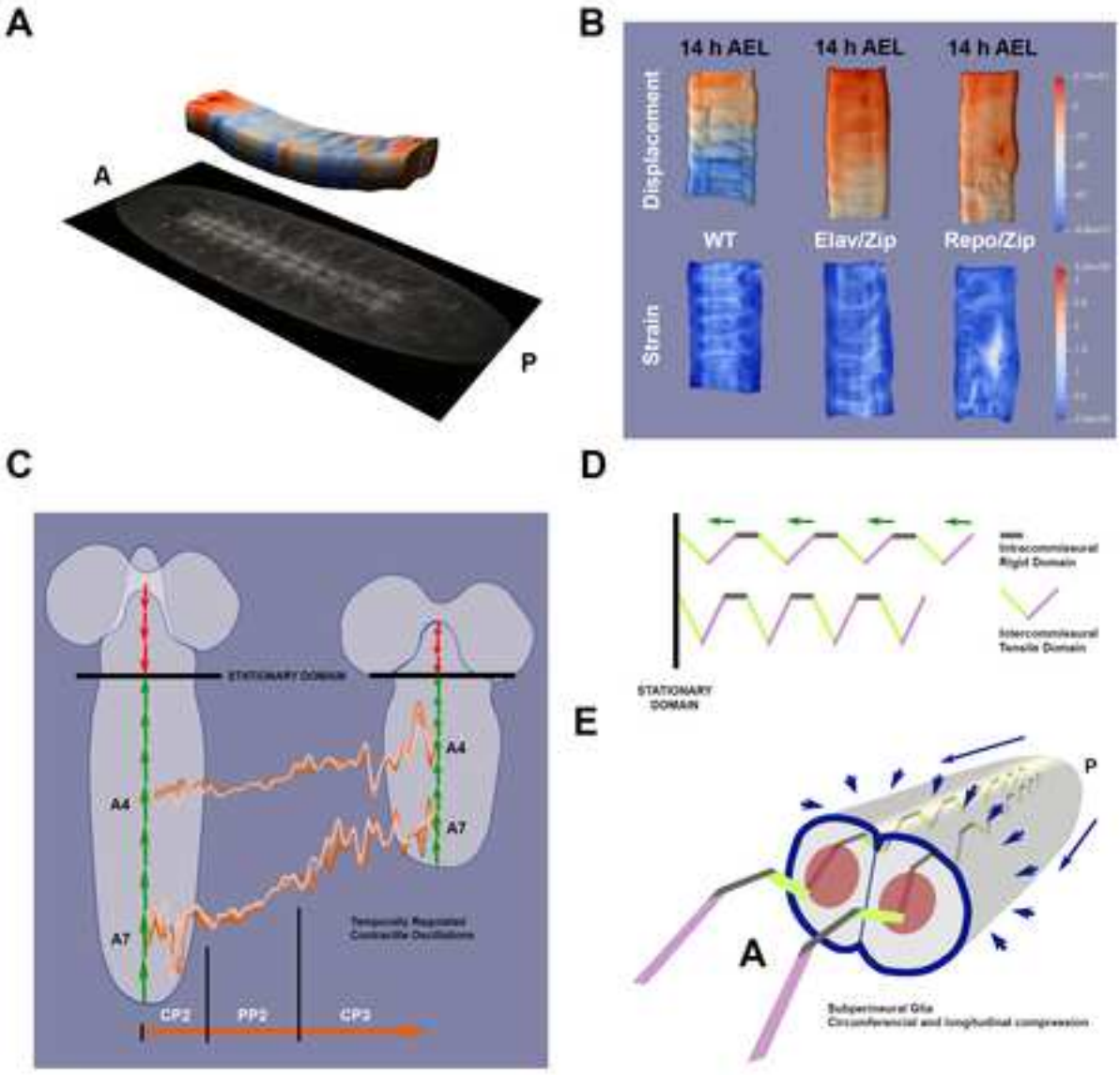

# Figure S1

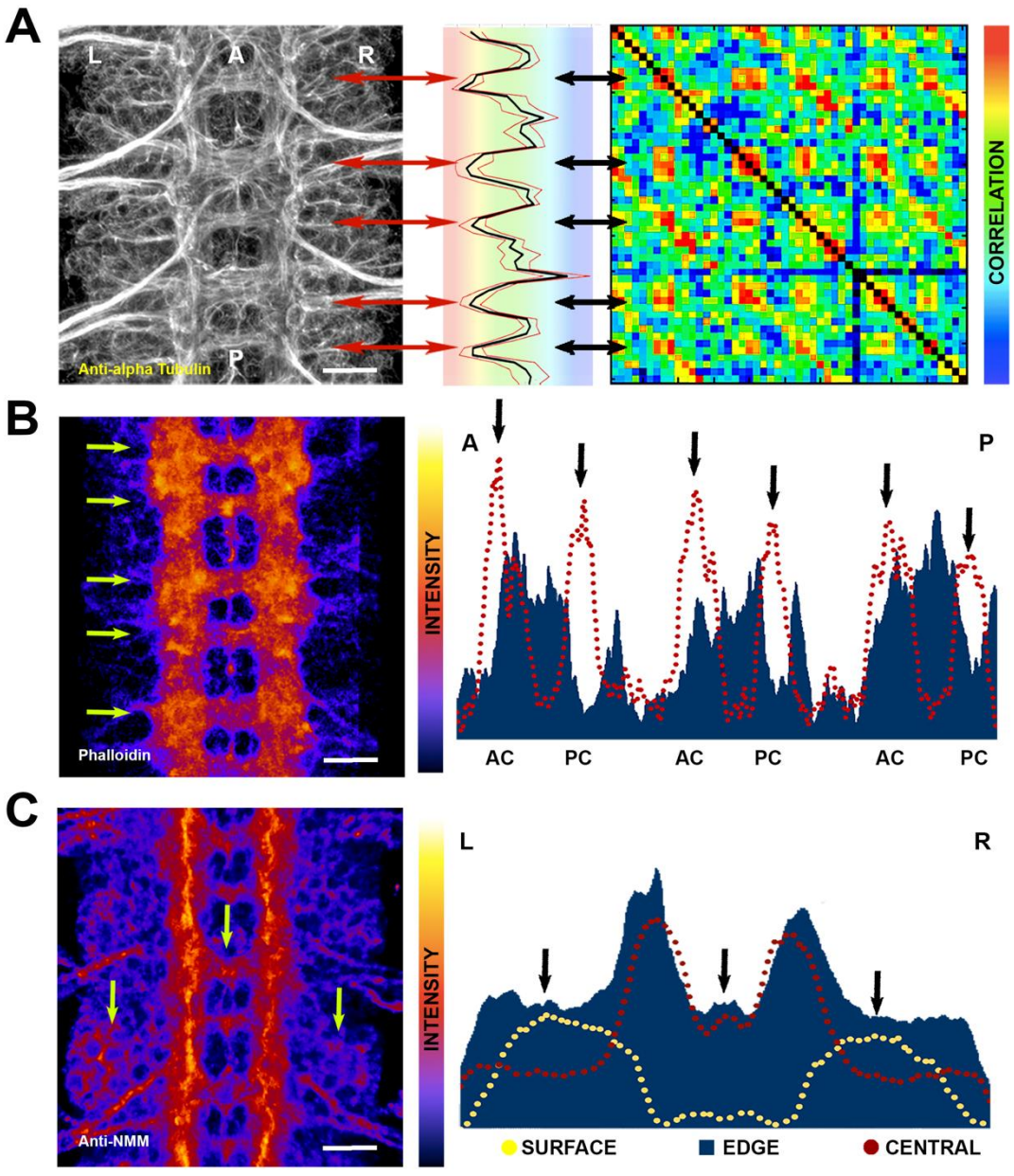
A
L
A
R
P
Anti-alpha Tubulin
CORRELATION
B
Phalloidin
INTENSITY
A
P
AC
PC
AC
PC
AC
PC
C
Anti-NMM
INTENSITY
L
R
SURFACE
EDGE
CENTRAL

**Figure S1: VNC Cytoskeleton structural organization, Related to Figure 6 and Correlation Data Analysis in the STAR Methods**

**A)** Acetylated α-Tubulin immunoreactivity. Left; maximum projection of a ventral view of three abdominal segments (A2 to A4) of the VNC of a 16-stage embryo. Left (L) and Right (R) and Anterior (A) and Posterior (P) orientation are labelled. Scale Bar is 10 μm. Middle; image cross-correlation score [mean (black) and ± standard deviation (red)] along the AP axis. Right; self cross-correlation matrix of the Z sections of the same image. The color-coded representation shows the correlation level (red-maximum to blue-minimum) for each possible cross comparison at each position of the image divided in 50 bins (see STAR Methods). Two axonal nodes with robust maximum correlation are conserved from segment to segment. **B)** Phalloidin (Actin) distribution. Left; maximum projection of a ventral view of three abdominal segments (A2 to A4) of the VNC of a 16-stage embryo. Signal Intensity is color coded (Fire LUT). Arrows point to the anterior and posterior commissures. Scale Bar is 10 μm. Right; Actin intensity profile along the AP axis: Discontinued Red at the ventral midline highlighting the anterior (AC) and posterior commissures (PC) (arrows). Solid Blue at the main contralateral trunks uncovering a stereotyped segmentally iterated distribution. **C)** Non-Muscle Myosin (NMM - Myosin II) imunoreactivity. Left; maximum projection of a ventral view of three abdominal segments (A2 to A4) of the VNC of a 16-stage embryo. Signal Intensity is color coded (Fire LUT). Arrows point to the lateral (left and right) and central neuropile domains. Scale Bar is 10 μm. Right; NMM intensity profile transversal to the AP axis: Discontinued Yellow at the ventral surface of the VNC highlighting the NMM accumulation at the lateral domains around the neurons cell bodies; Solid Blue at the medial edge of the longitudinal axonal trunks showing the preferential acumulation of NMM at contralateral single-cell domains at the dorsomedial edge; and Discontinued Red at the middle of the VNC trunk. See also **Movie S1**.

# Figure S2

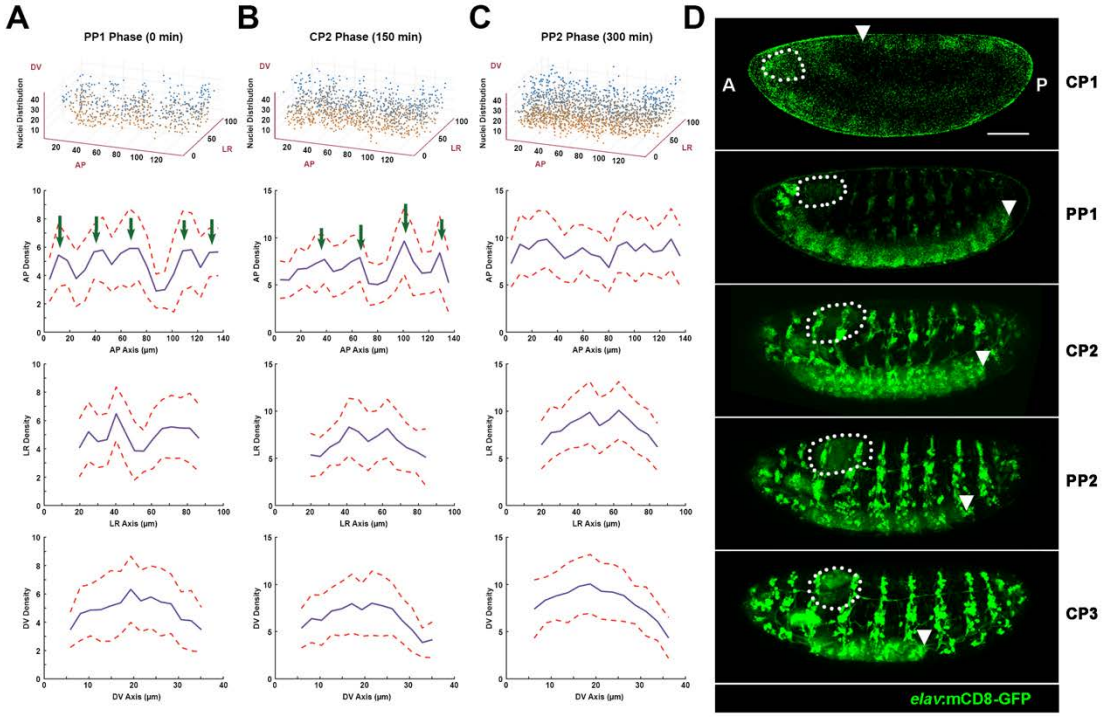
A
PP1 Phase (0 min)
B
CP2 Phase (150 min)
C
PP2 Phase (300 min)
D
DV
AP
LR
Nuclei Distribution
AP Density
LR Density
DV Density
AP Axis (μm)
LR Axis (μm)
DV Axis (μm)
A
P
CP1
PP1
CP2
PP2
CP3
elav:mCD8-GFP

**Figure S2: VNC condensation temporal development and spatial distribution of cell density, Related to Figure 1 and Neuronal cell bodies Semi-Automated Segmentation and Cell Density Estimation in the STAR Methods**

Density of neurons cell bodies along condensation progression: **A)** PP1 phase; **B)** CP2 phase; **C)** PP2 phase. Top row: 3D representation of the spatial position of the neurons cell nucleus at the respective time points, with color coding representing height along the DV-axis. Second row: Average number of nuclei neighbouring each nucleus (AP density) along the AP axis. Third row: Average number of nuclei neighbouring each nucleus along the left-right (LR) axis. Fourth row: Average number of nuclei neighbouring each nucleus along the DV axis. In all panels the blue curve is mean and the dashed red line represent ±1 s.d. Green arrows denote peaks in the density. **D)** Snapshots corresponding to the five phases of VNC condensation (CP1, PP1, CP2, PP2, CP3) from a time lapse (Movie S2) of an Elav-Gal4>UAS-mCD8-GFP embryo (lateral view) recorded by confocal microscopy. mCD8-GFP labelling marks all neural derivatives. Dotted shapes indicate the position of the brain lobes. Arrowheads denote the posterior tip of the VNC. AP axis orientation is indicated. Scale bar 50μm. We calculated the nuclei density by quantifying the number of nuclei that were within a sphere of radius 7.5mm from each nucleus. We did not calculate the density for nuclei near the tissue edges to minimize boundary effects.

# Figure S3

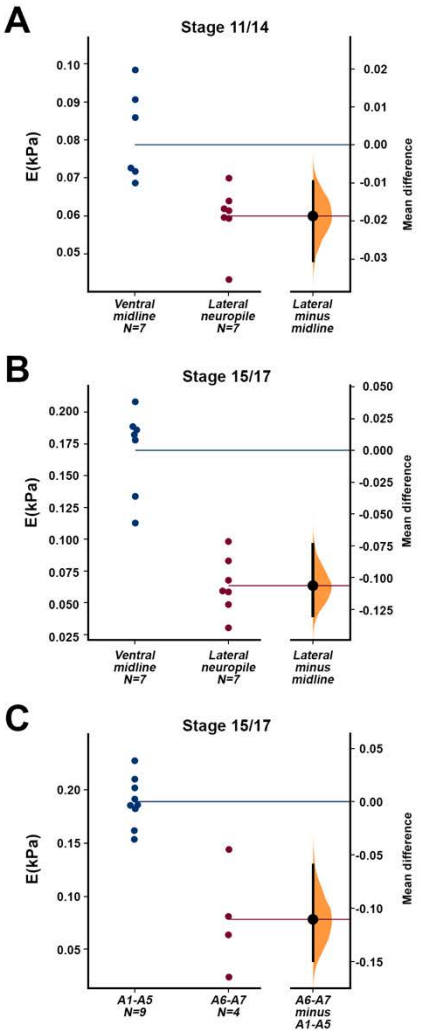
A
Stage 11/14
E(kPa)
Mean difference
Ventral midline N=7
Lateral neuropile N=7
Lateral minus midline
B
Stage 15/17
E(kPa)
Mean difference
Ventral midline N=7
Lateral neuropile N=7
Lateral minus midline
C
Stage 15/17
E(kPa)
Mean difference
A1-A5 N=9
A6-A7 N=4
A6-A7 minus A1-A5

**Figure S3: Quantification of VNC material properties during condensation, Related to Figure 2**

**A)** Statistical analysis of measured E (stiffness values) at different positions from stage 11-14 (estimationstats.com). Data points are shown on the left. The confidence interval is shown on right. $p < 0.05$ from Mann-Witney test. **B)** As **A**, but for late stages 15-17. $p < 10\text{-}2$ from Mann-Witney test. **C)** As **B**, but comparing the E measured in anterior domains (A1-A5) with those of posterior domains (A6-A7). $p < 10\text{-}2$ from Mann-Witney test.

# Figure S4

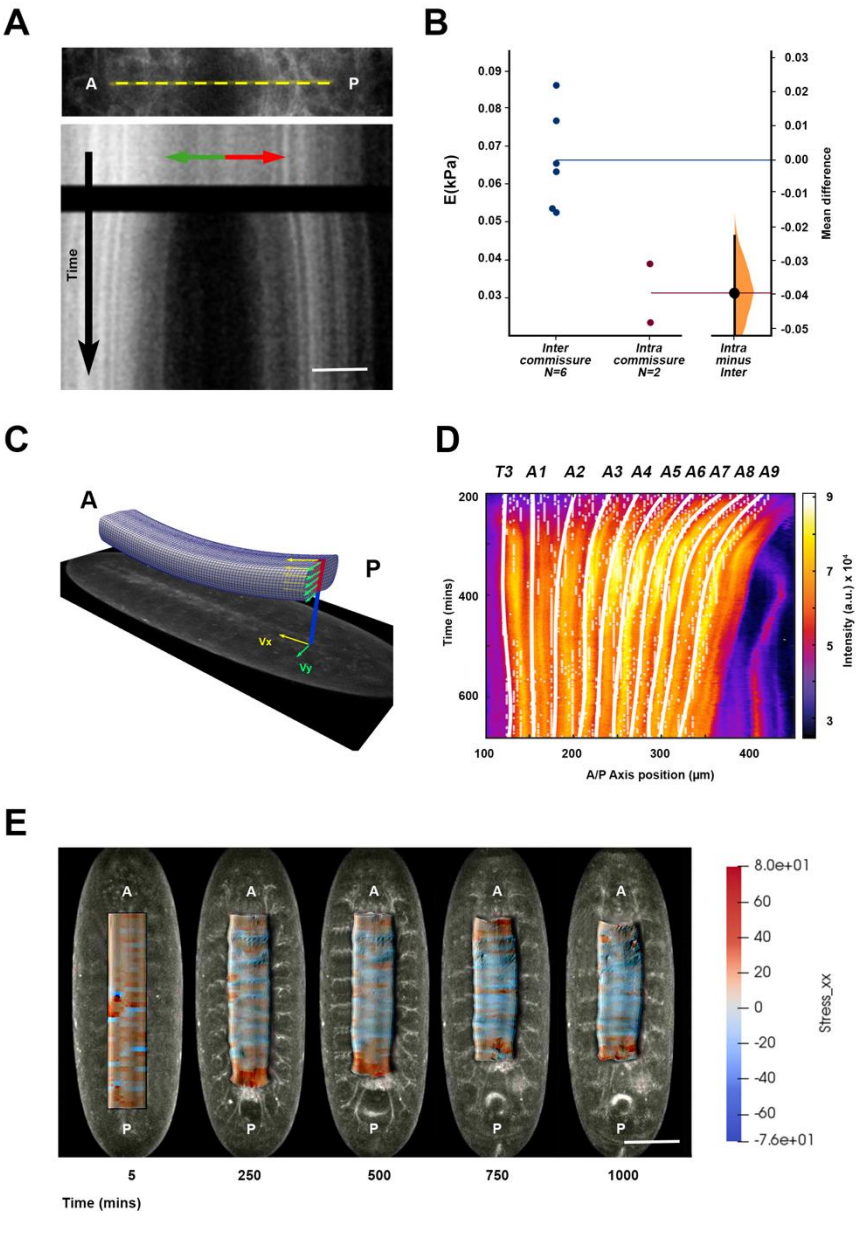
A
A
P
Time
B
E(kPa)
0.09
0.08
0.07
0.06
0.05
0.04
0.03
Mean difference
0.03
0.02
0.01
0.00
-0.01
-0.02
-0.03
-0.04
-0.05
Inter commissure N=6
Intra commissure N=2
Intra minus Inter
C
A
P
Vx
Vy
D
T3 A1 A2 A3 A4 A5 A6 A7 A8 A9
Time (mins)
200
400
600
100
200
300
400
A/P Axis position (µm)
Intensity (a.u.) x 10⁴
9
7
5
3
E
A
P
5
250
500
750
1000
Time (mins)
8.0e+01
60
40
20
0
-20
-40
-60
-7.6e+01
Stress_xx

**Figure S4: Analyses of laser microsurgery of the VNC and details of the finite elements model, Related to Figures 3 and 4**

**A)** (Top) VNC tissue recoil after generating a laser cut perpendicular to the AP axis of a stage 14 embryo expressing alpha Tubulin-GFP. Yellow dashed line indicates the region of analysis. (Bottom) Kymograph of VNC recoil after laser ablation. Green (anterior) and red (posterior) arrows indicate tissue recoil directionality. The black transversal domain spans the period of laser cutting. Scale bar 10 μm. **B)** Analysis of VNC recoil speed, at inter- and intracommissural domains. Confidence interval on right. Generated using estimationstats.com. **C)** Mapping of the measured velocities from PIV onto the FE model. Each velocity on the (x, y) plane is mapped onto points of the deformed mesh with closer (x, y) positions. Nodes with non-associated velocity were deformed according to Cauchy's equilibrium equation for a viscoelastic material and discretized (see STAR Methods). **D)** As **Figure 3F**, but showing the points of maximum compression (minimum value of $\sigma''''$) before (white dots) and after smoothing (white lines). **E)** Snapshots of deformed FE model showing contour plot of the AP normal stress $\boldsymbol{\sigma_{xx}}$ superimposed over the corresponding images (ventral view) of Fas2-GFP embryos. Scale bar 50 μm.

# Figure S5

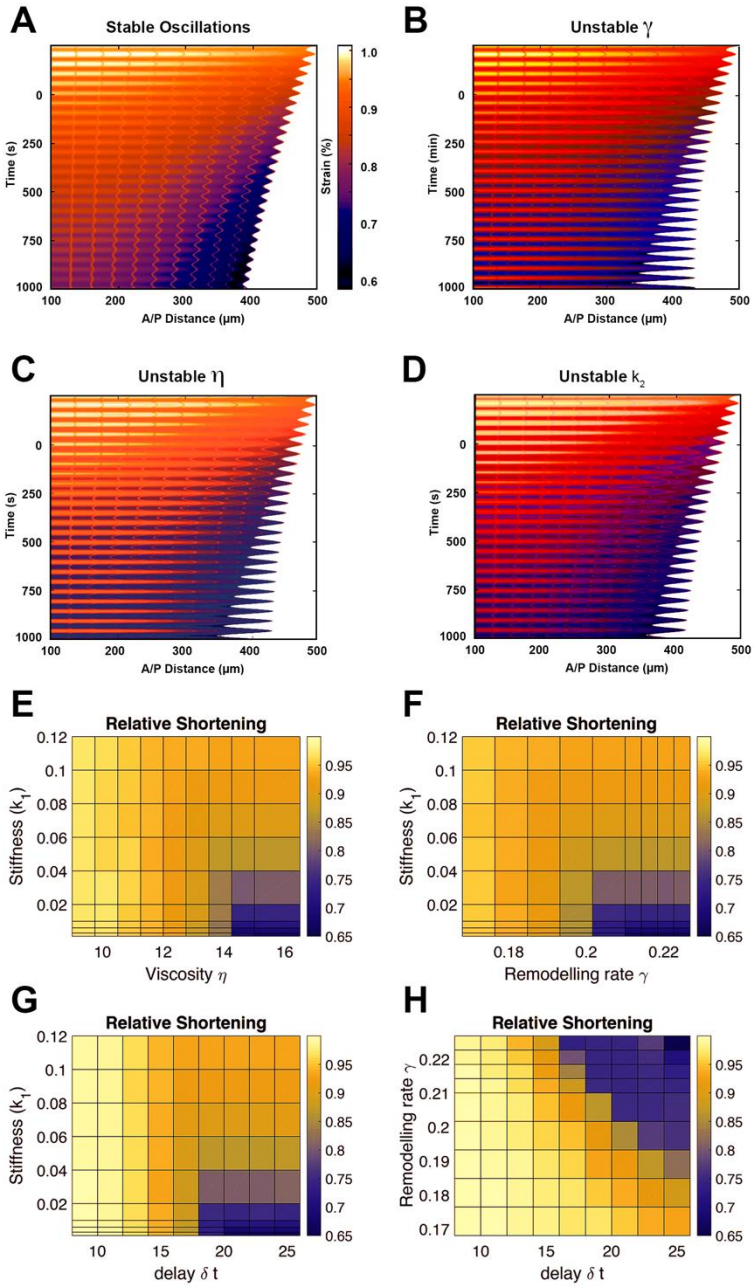
A
Stable Oscillations
Time (s)
A/P Distance (μm)
Strain (%)
B
Unstable γ
Time (min)
A/P Distance (μm)
C
Unstable η
Time (s)
A/P Distance (μm)
D
Unstable k2
Time (s)
A/P Distance (μm)
E
Relative Shortening
Stiffness (k1)
Viscosity η
F
Relative Shortening
Stiffness (k1)
Remodelling rate γ
G
Relative Shortening
Stiffness (k1)
delay δ t
H
Relative Shortening
Remodelling rate γ
delay δ t

**Figure S5: Kymographs of rest-length and condensation diagrams on four planes of the parameter space, Related to Figure 4**

**A-D)** Rheological model with delay using different material parameters and numerical simulation **A)** Stable oscillation using reference values: remodeling rate $\gamma = 0.21\ s^{-1}$, viscous friction $\eta = 15$ Pa.s., delay $\Delta t = 20$ s, and stiffnesses $k_1 = 0.01$ Pa and $k_2 = 1.9$ Pa, respectively. Initial rest-length is $L_0 = 0.95 l_0$, with $l_0$ being the initial apparent length. **B)** Unstable oscillations due to increase of remodeling rate ($\gamma = 0.22\ s^{-1}$). **C)** Unstable oscillations due to increase of viscosity $\eta$=16 Pa.s. **D**) Unstable oscillations due to decrease of stiffness $k_2$ =1.8 Pa. **E-H)** Relative shortening measured as the relative final length, $l_{final}/l_0$, for different combinations of perturbed values of model parameters: elastic stiffness $k_1$, viscosity $\eta$, delay $\delta t$, and remodeling rate $\gamma$. **A)** Stifness / Viscosity. **B)** Stifness / Remodeling rate. **C)** Stifness / Delay time. **D)** Remodeling rate / Delay time. Values have been chosen around the reference parameters ($k_1$, $\eta$, $\delta t$, $\gamma$) = (0.01, 15, 20, 0.2). Effects of stiffness $\kappa_2$ of viscoelastic branch are similar to those of $k_1$.

# Figure S6

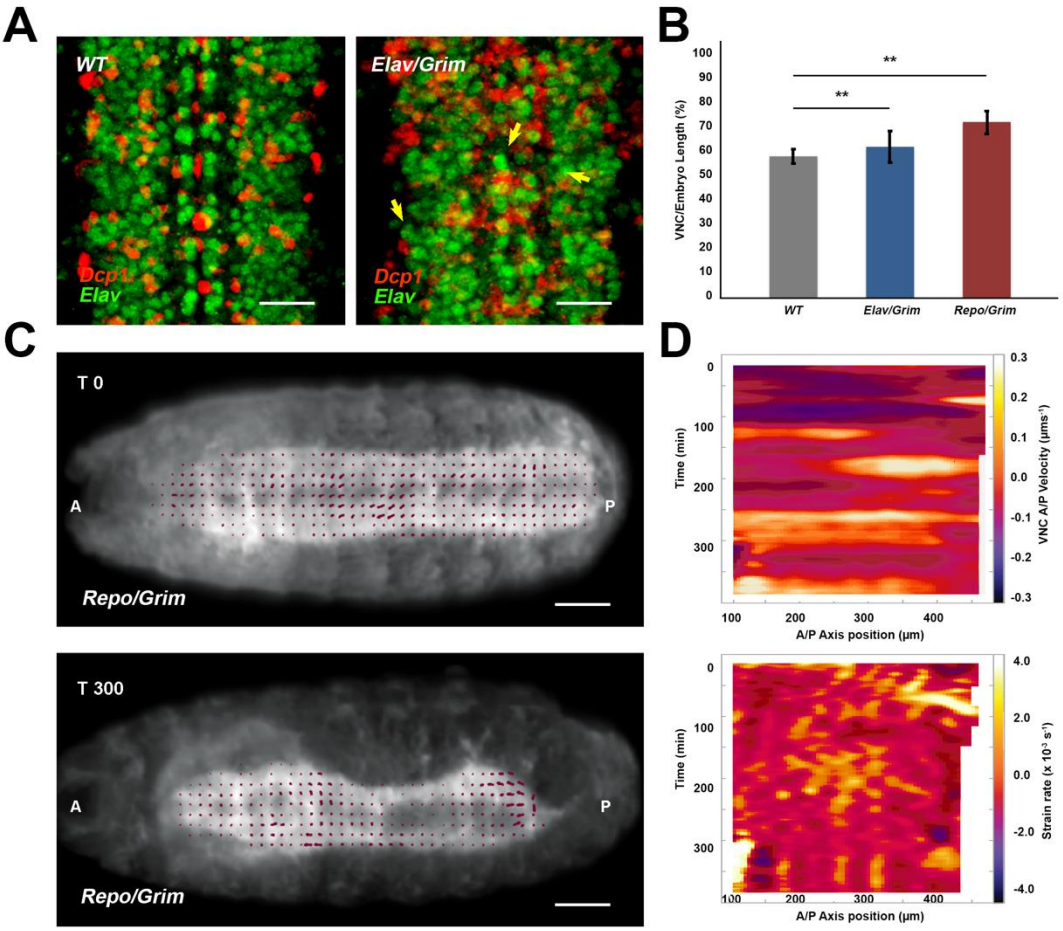
A
WT
Dcp1
Elav
Elav/Grim
Dcp1
Elav
B
VNC/Embryo Length (%)
**
**
WT
Elav/Grim
Repo/Grim
C
T 0
A
P
Repo/Grim
T 300
A
P
Repo/Grim
D
Time (min)
A/P Axis position (μm)
VNC A/P Velocity (μms⁻¹)
Time (min)
A/P Axis position (μm)
Strain rate (x 10⁻³ s⁻¹)

**Figure S6: Large-scale forces and local tissue dynamics are modulated by neurons and glia, Related to Figure 5**

**A)** CNS Flat-preps of WT (top) and Elav-Gal4>UAS-Grim (bottom) embryos, at stage 16, immunostained for Dcp1 (red) and Elav (green). Yellow arrowheads point to ELAV positive, Dcp1 negative cells, which are neurons that have not engaged to apoptosis. Scale bar 10 μm. **B)** Quantification of VNC length (VNC/Embryo Length %) of WT (gray), Elav-Gal4>UAS-Grim (blue) and Repo-Gal4>UAS-Grim (red) embryos, at stage 16. Bars represent mean values (n=6 embryos). **$p < 10^{-2}$. **C)** Snapshots from light-sheet imaging recordings of a Repo-Gal4::UAS-mCD8-GFP::His2Av-mRFP>UAS-Grim embryo (ventral view) at two different times of development (Stages 15-17) **(Movie S6)**. Magenta arrows denote local velocity trajectories from PIV analyses. AP axis orientation is indicated. Scale bar 50 μm. **D)** Velocity (as in **Figure 1C**) and strain rate (as in **Figure 2D**) kymographs for a representative Repo-Gal4>UAS-Grim embryo. No periodic oscillations were observed.

# Figure S7

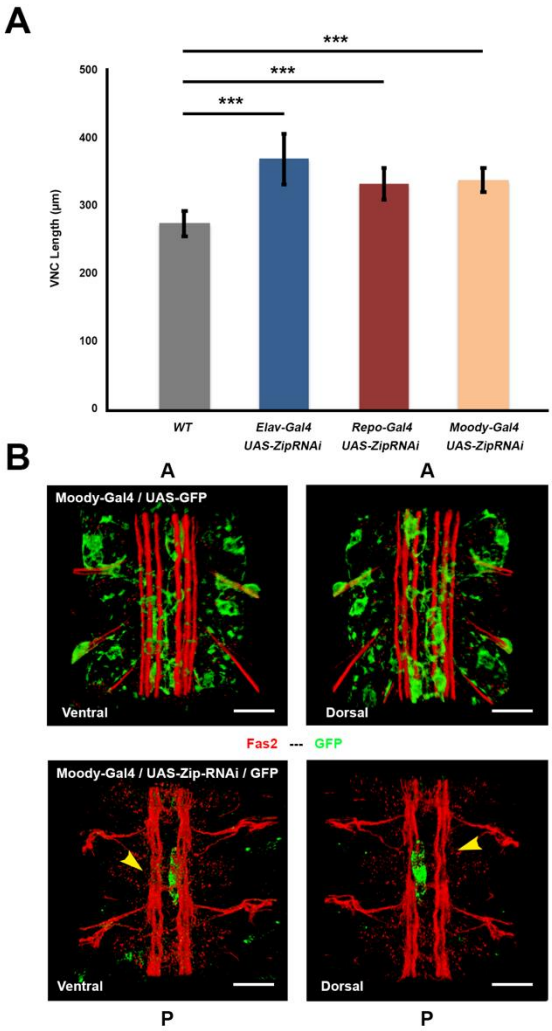
A
***
***
***
500
400
300
200
100
0
VNC Length (µm)
WT
Elav-Gal4 UAS-ZipRNAi
Repo-Gal4 UAS-ZipRNAi
Moody-Gal4 UAS-ZipRNAi
B
A
A
Moody-Gal4 / UAS-GFP
Ventral
Dorsal
Fas2 --- GFP
Moody-Gal4 / UAS-Zip-RNAi / GFP
Ventral
Dorsal
P
P

**Figure S7: Subperineural glia contractility is necessary for condensation and VNC organization, Related to Figure 6**

**A)** Quantification of VNC length of WT (gray), Elav-Gal4>UAS-Zip-RNAi (blue), Repo-Gal4>UAS-Zip-RNAi (red) and Moody-Gal4>UAS-Zip-RNAi embryos (orange), at stage 16. Bars represent mean values (n = 5 embryos). ***p < 10-3. **B)** Ventral and Dorsal 3D views of dissected, stage 16, control (top) and Moody-Gal4::UAS-mCD8-GFP>UAS-Zip-RNAi (bottom) embryos, immunostained for Fas2 (red) and GFP (green). Yellow arrowheads point to the disrupted axonal network. AP axis orientation is indicated. Scale bar 10 μm.